10

Cadmium (Zinc) Telluride 2D/3D Spectrometers for Scattering Polarimetry

Rui Miguel Curado da Silva, Ezio Caroli, Stefano del Sordo, and Jorge M. Maia

CONTENTS

10.1 Introduction 241
10.2 X- and γ-Rays Spectroscopy with CZT/CdTe Sensors 243
10.2.1 CdTe/CZT as X- and γ-Rays Spectrometer 244
10.2.2 Spectroscopic Performance Improvement Techniques 249
10.3 CZT/CdTe Spectrometers with 3D Spatial Resolution 251
10.3.1 Pixel Spectrometers with Coplanar Guard Grid 253
10.3.2 PTF Microstrip with Drift Configuration 255
10.4 CZT/CdTe Spectro-Imagers for Compton Polarimetry in Astrophysics 261
10.4.1 Compton (or Scattering) Polarimetry Principle 262
10.4.2 Polarimetry Modulation in CdTe/CZT Pixel Spectrometers 265
10.4.2.1 Synchrotron Beamline Optical System 265
10.4.2.2 CdZnTe Detection System 266
10.4.2.3 Shaping and Coincidence Electronic Subsystems 266
10.4.2.4 Data Acquisition Unit 266
10.4.3 Polarimetry Optimization of CdTe/CZT Pixel Detector 270
10.5 Consideration on CZT/CdTe Spectroscopic-Imager Applications and Perspective for Scattering Polarimetry 276
References 278

10.1 Introduction

The semiconductor detectors technology has dramatically changed the broad field of x- and γ-rays spectroscopy and imaging. Semiconductor detectors, originally developed for particle physics applications, are now widely used for x/γ-rays spectroscopy and imaging in a large variety of fields, among which, for example, x-ray fluorescence, γ-ray monitoring and localization, noninvasive inspection and analysis, astronomy, and diagnostic medicine. The success of semiconductor detectors is due to several unique

characteristics as the excellent energy resolution, the high detection efficiency, and the possibility of development of compact and highly segmented detection systems (i.e., spectroscopic imager). Among the semiconductor devices, silicon (Si) detectors are the key detectors in the soft x-ray band (<15 keV). Si-PIN diode detectors (Pantazis et al. 2010) and silicon drift detectors (SDDs; Lechner et al. 2004), operated with moderate cooling using small Peltier cells, show excellent spectroscopic performance and good detection efficiency below 15 keV. On the other side, germanium (Ge) detectors are unsurpassed for high-resolution spectroscopy in the hard x-ray energy band (>15 keV) and will continue to be the first choice for laboratory-based high-performance spectrometers system (Eberth and Simpson 2006).

However, in the last decades, there has been an increasing demand for the development of room-temperature detectors with compact structure having the portability and convenience of a scintillator, but with a significant improvement in energy resolution and/or spatial resolution. To fulfill these requirements, numerous high-*Z* and wide bandgap compound semiconductors have been exploited (Owens and Peacock 2004; Sellin 2003). As demonstrated by the impressive increase in the scientific literature and technological development, cadmium telluride (CdTe) and cadmium zinc telluride (CZT) based devices are today dominating the room-temperature semiconductor applications scenario, being widely used for the development of x/γ-ray instrumentation (Lebrun et al. 2003; Lee et al. 2010; Ogawa and Muraishi 2010) in different application fields.

Sellin 2003 is not in the reference list. Please provide complete publication details to be added in the reference list or delete citation.

In particular, applications that require imaging capabilities with high spatial resolution possibly coupled with good spectroscopic performance (at room temperature) are certainly the field in which CdTe/CZT sensors technology can exploit all its potential and advantages. In fact, the possibility to easily segment the charge collecting electrodes into strips and/or arrays, as well as to assemble mosaics of even small sensitive units (i.e., crystals), allow one to obtain devices with excellent bi-dimensional spatial resolution (down to tens of microns). According to the type of readout electronics, these devices allow the accurate measure of the energy released by the interaction of photons within the material (Limousin et al. 2011; Watanabe et al. 2009; see also other chapters in this book).

One quite new and challenging application field for CdTe/CZT spectro-imagers is x- and γ-rays polarimetry. This type of measurement is becoming increasingly important in high-energy astrophysics. Until now, polarimetry in high-energy astrophysics has been an almost unexplored field due to the inherent difficulty of the measurement and also to the complexity of the required detection, electronic, and signal processing systems, since celestial x/γ-ray sources are only observable from space. To date, x- and γ-ray cosmic source emissions have been studied exclusively through traditional spectral and timing analysis, and imaging of the measured fluxes.

Polarization measurements will increase the number of observational parameters of the same x/γ-ray source by two: the polarization angle and

the level of linear polarization. These additional parameters should allow a better discrimination between different emission models characterizing the same object. Polarimetric observations can provide fundamental information about the geometry, the magnetic field, and the active emission mechanisms of cosmic-ray sources, helping to solve several hot scientific issues. For these reasons, the high-energy polarimetric capability is currently recognized as an essential requirement for the next generation of space telescopes.

In the range 10–1000 keV, effective polarization measurements can be performed by using the properties of Compton scattering for polarized photons. A spectroscopic imager made of CZT/CdTe offers a suitable and high-performance solution to build a scattering polarimeter (Caroli et al. 2000). Furthermore, this solution offers the capability to perform polarization measurements simultaneously with those of spectroscopy, imaging, and timing. This represents a major advantage for new space instruments, both for the optimization of payload and inflight resources utilization and for the scientific return, because the various observational parameters on the same source can be correlated without problems due to the time variability of the sources itself and/or background.

The chapter is divided into two main parts. The first part, comprising Sections 10.2 and 10.3, gives a summary of room-temperature semiconductor principle and CZT/CdTe development for the realization of detectors for x- and γ-rays suitable for building two- and three-dimensional spectroscopic imagers (Caroli and Del Sordo 2015). The second part is dedicated to addressing a very hot and challenging topic: the use of CdTe/CZT spectroscopic imagers as scattering polarimeters for high-energy astrophysics applications and is mainly based on the results obtained by the authors and colleagues both by experiments and by Monte Carlo simulations.

10.2 X- and γ-Rays Spectroscopy with CZT/CdTe Sensors

The typical operation of semiconductor detectors is based on collection of the charges, created by photon interactions, through the application of an external electric field. The energy range of interest mainly influences the choice of the best semiconductor material for a radiation detector. Among the various interaction mechanisms of x- and γ-rays with matter, three effects play an important role in radiation measurements: photoelectric absorption, Compton scattering, and pair production (Leo 1994). In photoelectric absorption, the photon transfers all its energy to an atomic electron, while a photon interacting through Compton process transfers only a fraction of its energy to an outer electron, producing a hot electron and a degraded photon. In pair production, a photon with energy above a threshold energy of 1.02 MeV interacts within the Coulomb field of the nucleus,

producing an electron–positron pair. Neglecting the escape of characteristic x-rays from the detector volume (the so-called fluorescent lines), only the photoelectric effect results in the total absorption of the incident energy and thus gives the correct information on the impinging photon energy. The interaction cross sections are highly dependent on the atomic number. In photoelectric absorption, it varies as $Z^{4,5}$, Z for Compton scattering and Z^2 for pair production.

10.2.1 CdTe/CZT as X- and γ-Rays Spectrometer

An optimum spectroscopic detector must favor photoelectric interactions, and so semiconductor materials with a high atomic number are preferred. Figure 10.1a shows the linear attenuation coefficients, calculated by using tabulated interaction cross-section values (Berger et al. 2010), for photoelectric absorption and Compton scattering of Si, CdTe, HgI_2, NaI, and BGO; NaI and BGO are solid scintillator materials typically used in radiation measurements. As shown in Figure 10.1a, photoelectric absorption is the main process up to about 200 keV for CdTe. The efficiency for CdTe detectors versus detector thickness for various typical photon energies is reported in Figure 10.1b. A 10 mm thick CdTe detector ensures good photoelectric efficiency at 140 keV (>95%), while a 1 mm thick CdTe detector is characterized by a photoelectric efficiency of 100% at 40 keV. It is important to note for the scope of this chapter that for all high-Z semiconductors, the Compton cross section becomes comparable with the photoelectric one over 200 keV.

Semiconductor detectors for x- and γ-rays spectroscopy behave as solid-state ionization chambers operated in pulse mode. The simplest configuration is a planar detector, i.e., a slab of a semiconductor material with metal electrodes on the opposite faces of the semiconductor (Figure 10.2a). Photon interactions produce electron–hole pairs in the semiconductor volume through the above-discussed interactions. The interaction is a two-step process where the electrons created in the photoelectric or Compton process lose their energy through electron–hole pair production. The number of electron–hole pairs is proportional to the released photon energy. If E is the released photon energy, the number of electron–hole pairs N is equal to E/w, where w is the average energy for pair creation. The generated charge cloud is $Q_0 = eE/w$. The electrons and holes move toward the opposite electrodes, anode, and cathode for electrons and holes, respectively (Figure 10.2a).

The movement of the electrons and holes causes variation ΔQ of induced charge on the electrodes. It is possible to calculate the induced charge ΔQ by the Shockley–Ramo theorem (Cavalleri et al. 1997; He 2001), which makes use of the concept of a weighting potential defined as the potential that would exist in the detector with the collecting electrode held at unit potential, while holding all other electrodes at zero potential. According to the

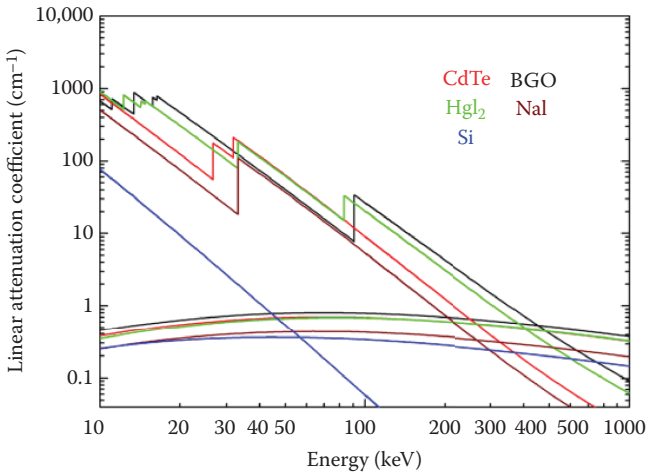

(a)

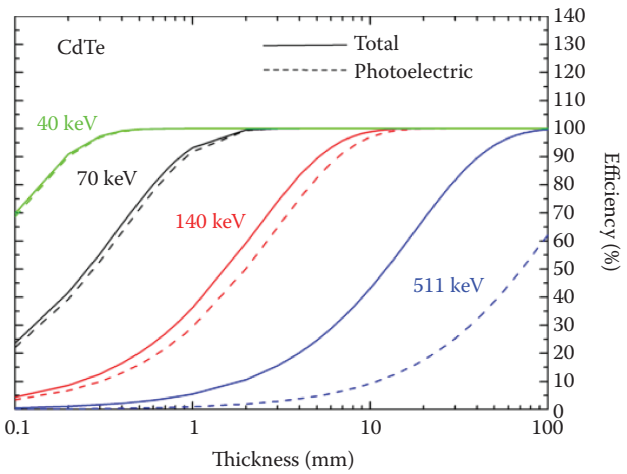

(b)

FIGURE 10.1
(a) Linear attenuation coefficients for photoelectric absorption and Compton scattering of CdTe, Si, HgI_2, NaI, and BGO. (b) Efficiency of CdTe detectors as function of detector thickness at various photon energies.

Shockley–Ramo theorem, the induced charge by a carrier q, moving from x_i to x_f, is

$$\Delta Q = -q[\varphi(x_f) - \varphi(x_i)] \tag{10.1}$$

where $\varphi(x)$ is the weighting potential at position x. The analytical solution of the Laplace equation inside the detector enables calculating the weighting

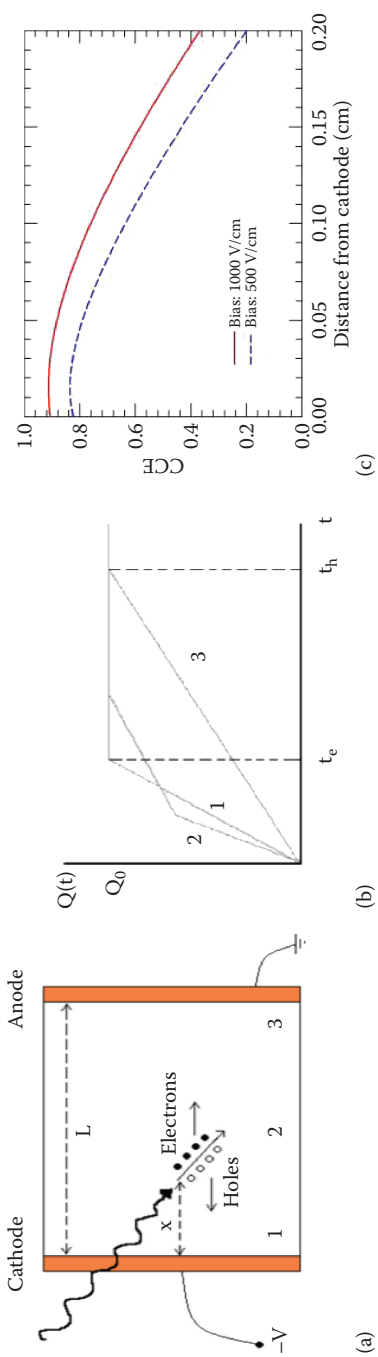

FIGURE 10.2
Planar configuration of a semiconductor detector. (a) Electron–hole pairs, generated by radiation, are swept toward the appropriate electrode by the electric field. (b) Time dependence of the induced charge for three different interaction sites in the detector (positions 1, 2, and 3). The fast rising part is due to the electron component, while the slower component is due to the holes. (c) CCE of a CZT planar detector (2 mm thick) evaluated by the Hecht equation for two different bias (i.e., electric field values) and for $\mu_e\tau_e$ and $\mu_h\tau_h$ equal to 1×10^{-3} cm^2/V and 8×10^{-5} cm^2/V, respectively.

potential (Eskin et al. 1999). In a semiconductor, the total induced charge is given by the sum of the induced charges due both to the electrons and holes.

Charge trapping and recombination are typical effects in compound semiconductors and may prevent full charge collection. For a planar detector, having a uniform electric field, neglecting charge detrapping, the charge collection efficiency (CCE), i.e., the induced charge normalized to the generated charge (Figure 10.2c), can be evaluated by the Hecht equation (Hecht 1939) and derived models (Zanichelli et al. 2013) and is strongly dependent on the photon interaction position. This dependence coupled with the random distribution of photon interaction points inside the sensitive volume increases the fluctuations on the induced charge and produces peak broadening in the energy spectrum as well as the characteristic low tail asymmetry in the full energy peak shape observed in planar CdTe/CZT sensors.

Hecht 1939 is not in the reference list. Please provide complete publication details to be added in the reference list or delete citation.

The charge transport properties of a semiconductor, expressed by mobility-lifetime products for holes and electrons ($\mu_h\tau_h$ and $\mu_e\tau_e$), are key parameters in the development of radiation detectors. Poor mobility-lifetime products result in short mean drift length λ, and therefore small λ/L ratios, which limit the maximum thickness and energy range of the detectors. Compound semiconductors, generally, are characterized by poor charge transport properties due to charge trapping. Trapping centers are mainly caused by structural defects (e.g., vacancies), impurities, and irregularities (e.g., dislocations, inclusions). In compound (CdTe and CZT) semiconductors, $\mu_e\tau_e$ is typically of the order of 10^{-5}–10^{-3} cm^2/V, while $\mu_h\tau_h$ is usually much worse with values around 10^{-6}–10^{-4} cm^2/V. Therefore, the corresponding mean drift lengths of electrons and holes are 0.2–20 and 0.02–2 mm, respectively, for typical applied electric fields of 2000 V/cm (Sato et al. 2002).

The charge collection efficiency is a crucial property of a radiation detector and affects the spectroscopic performances and in particular the energy resolution. High charge collection efficiency ensures good energy resolution, which also depends on the statistics of the charge generation and on the noise of the readout electronics. Three contributions mainly affect the energy resolution (FWHM) of a radiation detector:

$$\Delta E = \sqrt{(2.355)^2 (F \cdot E \cdot w) + \Delta E_{el}^2 + \Delta E_{coll}^2} \tag{10.2}$$

The first contribution is the noise due to the statistics of the charge carrier generation, where F represents the Fano factor. In semiconductors, F is much smaller than unity (0.06–0.14) (Devanathan et al. 2006). The second contribution is the electronic noise, which is generally measured directly using a precision pulser, while the third term takes into account the contribution of the charge collection process. Different semi-empirical relations have been proposed for the charge collection contribution evaluation of different detectors (Kozorezov et al. 2005).

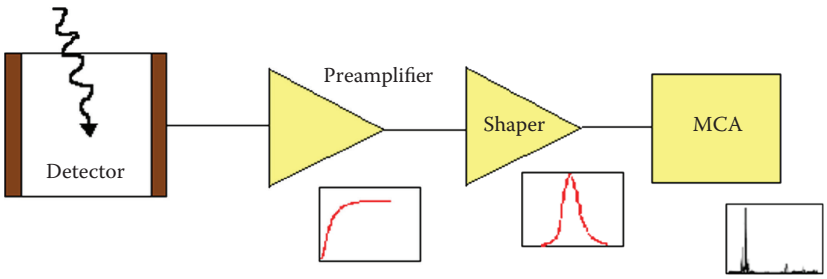

FIGURE 10.3
Block diagram of a standard spectroscopic detection system for x- and γ-rays.

Figure 10.3 shows the typical spectroscopic system based on a semiconductor detector. The detector signals are read out by a charge sensitive preamplifier (CSP) and then shaped by a linear amplifier. A multichannel analyzer (MCA), which samples and records the shaped signals, finally acquires and records the deposited energy spectrum.

As pointed out later, poor holes transport properties of CdTe and CdZnTe materials are a critical issue in the development of x- and γ-rays detectors. Hole trapping reduces the charge collection efficiency of the detectors and produces asymmetry and a long tail in the photopeaks in the measured spectra (holes tailing). In order to minimize this effect, several methods have been used. Some techniques concern the particular irradiation configuration of the detectors (Figure 10.4a). *Planar parallel field* (PPF) is the classical configuration used in overall planar device. In this configuration, the

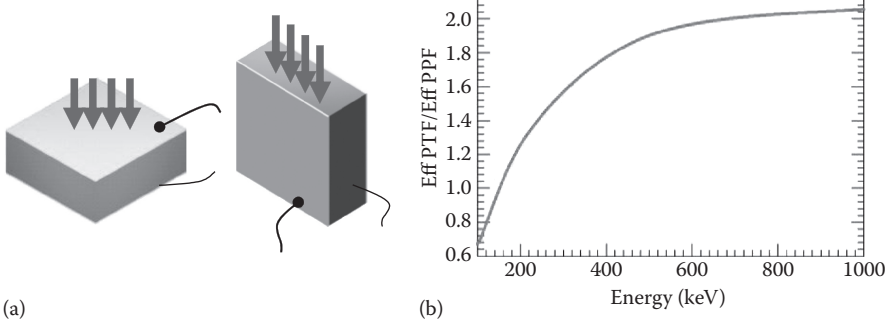

FIGURE 10.4
(a) Usual irradiation configuration in which photons impinge (arrows) the detector through the cathode surface (PPF: planar parallel field) and the PTF (planar transverse field), one in which the photons impinge on the sensor orthogonally with respect to the charge collecting field. (b) Ratio between PTF and PPF efficiency for impinging photon energies from 50 to 1000 keV assuming the PTF thickness equal to 10 mm and the distance between electrodes (i.e. the PPF absorption thickness) 2.5 mm.

irradiation of the detector is through the cathode electrode, thus minimizing the hole trapping probability. In an alternative configuration, denoted as *planar transverse field* (PTF) (Casali et al. 1992), the irradiation direction is orthogonal (transverse) to the electric field. In this irradiation condition, different detector thicknesses can be chosen to fit the detection efficiency required, without modifying the interelectrodes distance and then the charge collection properties of the detectors. This technique is particularly useful in developing detectors with high detection efficiency in the γ-ray energy range. In Figure 10.4b, the ratio is plotted between the efficiency achievable by a CdTe spectrometers with lateral sides of 10 mm and a distance between electrodes of 2.5 mm (Caroli et al. 2008). This plot shows that the PTF irradiation configuration starts to be convenient in terms of detection efficiency above 200 keV.

10.2.2 Spectroscopic Performance Improvement Techniques

To compensate for the trapping effects in CdTe/CZT semiconductor detectors, and therefore to improve their spectroscopic performance and increase their full energy efficiency, different methods have been proposed. The most used methods rely on the possibility of avoiding the contribution of holes on the formation of the charge signal and therefore using the CZT/CdTe detector as single charge sensing devices. In this configuration, only electrons are collected and, because their mobility-lifetime characteristics, the effect of trapping is limited and can be even more efficiently compensated by using simple signal manipulation. There are several techniques to realize single charge carrier (namely electrons) sensing CdTe and CdZnTe detectors (unipolar detectors). Some of these techniques are based on electronic methods (e.g., pulse rise time discrimination; Jordanov et al. 1996) and biparametric readout (Richter and Siffert 1992; Auricchio et al. 2005). While others rely on particular electrode design (e.g., Frisch-grid—McGregor et al. 1998; Bolotnikov et al. 2006; pixels—Barrett et al. 1995; Kuvvetli and Budtz-Jørgensens 2005; coplanar grids—Luke 1995; strips—Shor et al. 1999; Perillo et al. 2004; multiple electrodes—Lingren et al. 1998; Kim et al. 2004; Abbene et al. 2007). Figure 10.5 shows some electrode designs used for CdTe and CdZnTe unipolar detectors. Within the proposed unipolar electrode configuration, particularly interesting for their intrinsic imaging properties, pixels and microstrips sensors (Figure 10.5b, c) are also characterized by unipolar properties, when the ratio between charge collection distance and the pixel/strip pitch is large (≫1), i.e., the so-called small pixel effect.

Is the term "mobility-lifetime characteristics" correct as meant, or should the hyphen be changed to em dash?

In general, the almost unipolar characteristics of these detector configurations are due to the particular shape of the weighting potential: it is low near the cathode and rises rapidly close to the anode. According to this characteristic, the charge induced on the collecting electrode is proportional to the weighting potential, as stated by the Shockley–Ramo theorem, and its major contribution comes from the drift of charge carriers close to the anode,

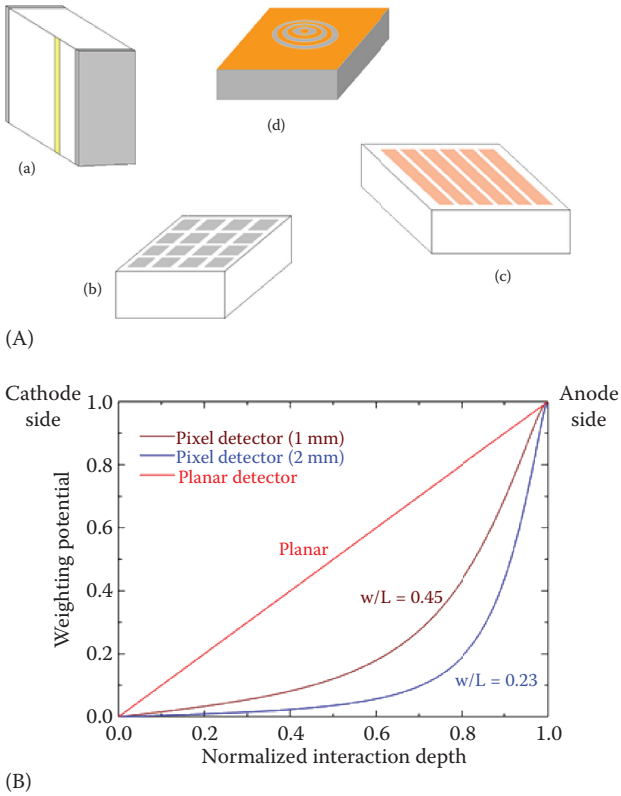

FIGURE 10.5
(A) Single charge sensing electrode configurations widely used in CdTe and CdZnTe detectors: (a) parallel strip Frisch grid, (b) pixel, (c) strip, and (d) multiple electrodes. (B) Weighting potential of a pixel detector, compared to a planar detector. It is possible to improve the unipolar properties of pixel detectors by reducing the w/L ratio (i.e., pixel size to detector thickness), according to the theory of small pixel effect.

i.e., the electrons. On the contrary, the linear shape of the weighting potential of a planar detector makes the induced charge sensitive to both electrons and holes, as discussed above.

In particular, the introduction of coplanar-grid noncollecting electrodes in the anode side design of sensors provides an important additional feature that is fundamental to realize 3D sensing spectrometers, that is, the position information of the radiation interactions point inside the sensitive volume (Luke 1995). In fact, for these electrode configurations, the induced charge on the planar cathode Q_p increases roughly as a linear function of the distance D of γ-ray interaction location from the coplanar anodes ($Q_p \propto D{\cdot}E_\gamma$) because it is proportional to the drift time of electrons. On the other hand, the coplanar anode signal Q_s is only approximately proportional to the γ-ray deposited energy ($Q_s \propto E_\gamma$). Therefore, the interaction depth can be estimated by

reading both Q_p and Q_s signal amplitude for each interaction through their ratio (also called depth parameter): $d = Q_p/Q_s \propto D$ (He et al. 1997).

10.3 CZT/CdTe Spectrometers with 3D Spatial Resolution

In this section, we focus on a particular type of detector based on sensitive elements of CZT/CdTe, namely spectrometers with spatial resolution in three dimensions. These devices represent the new frontiers for applications in different fields that require increasing performance such as high-energy astrophysics, environmental radiation monitoring, medical diagnostics with PET, and inspections for homeland security (Vetter et al. 2007; Gu et al. 2011; Whal et al. 2015).

A 3D spectrometer is a detector divided into volume elements (voxels), each operating as an independent spectroscopic detector. The charge produced in each voxel by the interaction of an incoming x/γ photon is converted into a voltage signal proportional to the released energy. If the readout electronics of the detection system implements a coincidence logic, it will be possible to determine to some extent (depending on the voxel dimensions and the time coincidence window) the history of the incident photon inside the sensitive volume by associating the energy deposits in more voxels to the same incident photon. These capabilities are of fundamental importance for applications requiring high-detection efficiency even at high energies (>200 keV), i.e., in the Compton scattering regime, as well as a wide-field localization of the direction of incidence and a uniform spectroscopic response throughout the sensitive volume. In fact, the possibility to reconstruct the photon interaction position in 3D will allow correcting from signal variations due to charge trapping and material non-uniformity and therefore will increase the sensitive volume of each detector unit without degrading the spectroscopic performance. A straightforward application of 3D spectro-imagers in hard x- and γ-rays is the realization of advanced Compton detectors that use the interaction position reconstruction with energy determination of each hit to evaluate the incoming photon direction through the Compton kinematic (Du et al. 2001; Mihailescu et al. 2007).

In the field of hard x-ray and soft γ-ray astrophysics (10–1000 keV), there are promising developments of new focusing optics operating for up to several hundreds of kiloelectron volts, through the use of broadband Laue lenses (Frontera et al. 2013; Virgilli et al. 2015) and new generation of multilayer mirrors (Della Monica Ferreira et al. 2013; Blozer et al. 2016). These systems make it possible to drastically improve the sensitivity of a new generation of high-energy space telescopes at levels far higher (i.e., 100 times) than current instrumentation. To obtain the maximum return from this type of optics up to megaelectron volts, focal plane detectors with high performance are

required. These detectors should guarantee at the same time high efficiency (>80%, at least) even at higher energies, fine spectroscopic resolution (1% at 500 keV), and also accurate localization (0.1–1 mm) of the interaction point of the photons used for the correct attribution of their direction of origin in the sky.

In fact, we should point out that 3D spectro-imager represents a promising way to realize highly efficient scattering polarimeters. This capability can finally open the hard x- and γ-rays polarimetry windows to space astronomy, making the measurement of the polarization of cosmic sources a standard observational mode, as it is now for imaging, spectroscopy, and timing, in the next generation of high-energy space telescopes.

The realization of 3D spectrometers by a mosaic of single CdTe/CZT crystals is not as easy as the case of bi-dimensional (2D) imagers. These difficulties are mainly due both to the small dimension of each sensitive unit necessary to guarantee the required spatial resolution and to the packaging of such 3D sensor units, requiring an independent spectroscopic readout electronics chain. A solution is the realization of a stack of 2D spectroscopic imagers (Watanabe et al. 2002; Judson et al. 2011). This configuration, while very appealing for large area detectors, has several drawbacks for applications requiring fine (<0.5 mm) spatial resolution in 3D and compactness (as focal plane detectors). Indeed, the distance between each 2D layer of the stack limits the accuracy and the sampling of the third spatial coordinate. Furthermore, passive materials normally required for mechanical support of each detection layer could introduce large amount of unwanted scatter.

To solve this kind of problem, in the last 10–15 years, several groups have focused their activity on the development of sensor units based on high-volume (1–10 cm^3) single crystals of CZT/CdTe capable of intrinsically operating as 3D spectrometers. The main target of these developments is to fulfill the requirements for a given application with only one high-performance sensor, and/or to make more efficient and easy the realization of 3D detectors based on matrices of these basic units. The main benefits of such approaches run from limitation of readout channel numbers to achieve the required spatial resolution to packing optimization with reduction of passive material between sensitive volumes. The adopted electrode configurations play a key role in these developments. As already seen in the previous section, various electrode configurations have been proposed and studied to improve both the spectroscopic performance and the uniformity of response of CZT/CdTe detectors. In fact, these electrode configurations, with the implementation of appropriate logical reading of the signals, make the sensors intrinsically able to determine the position of interaction of the photon in the direction of the collected charge (depth sensing) and therefore are particularly suited to the realization of 3D monolithic spectrometers without requiring a drastic increase in the electronics readout chains.

In the following sections, we describe, as examples, a couple of configurations currently proposed and under development for the realization of 3D

spectrometers based on single large volume crystals of CdTe/CZT. Within other undergoing developments (Cui et al. 2008; Bale and Szeles 2006; Owens et al. 2006; Dish et al. 2010; Macri et al. 2002, 2003; Luke 2000; Matteson et al. 2003), we report only on these two configurations which are intrinsically capable to fulfill requirements for fine spatial resolution in all three dimensions coupled with high and uniform spectroscopic response.

10.3.1 Pixel Spectrometers with Coplanar Guard Grid

By combining a pixelated anode array, already providing good energy resolution because of the small pixel effect introduced in Section 10.2.2, and an interaction depth sensing technique for electron trapping corrections, it is possible to build CdZnTe γ-ray spectrometers with intrinsic 3D position sensing capability over a quite large volume (1–3 cm^3) of bulk crystals (He et al. 1999).

The first prototype was based on a 10 × 10 × 10 cm^3 CZT crystal with an 11 × 11 pixel anode array and a single cathode electrode on the opposite surface (Stahle et al. 1997). The 2D sensing of γ-ray interactions is provided by the pixel (x, y) anode where electrons are collected. Instead of using an array of simple square pixel anodes, each collecting anode is surrounded by a common noncollecting grid (Figure 10.6a, b). The pixel pitch had a dimension of 0.7 × 0.7 mm^2, with a collecting anode of 0.2 × 0.2 mm^2 at the center surrounded by a common noncollecting grid with a width of 0.1 mm. Since the noncollecting grid is biased at lower potential relative to that of the collecting anodes, electrons are forced toward the collecting pixel anodes. Even more important, the dimension of the pixel anode is small with respect to the anode–cathode distance and smaller than the geometrical pixel dimension enhancing the small pixel effect and minimizing any induced signal from the holes movement. To guarantee a good electron collection, the bias voltage between anodes and the planar cathode is in the 1.5–2 kV range, while the voltage difference between anodes and the noncollecting common grid is typically of few tens of volt (30–50 V).

The ratio between the cathode and the anode signals allow determining the γ-ray interaction depth between the two electrodes planes. With a simple coincidence logic between cathode and anode signals, this technique can provide the depth (z) of the photon interaction for single-site events, and only the centroid depth for multiple-site interactions (e.g., Compton scattered events). The identification of individual hit depths for multiple-site events requires the readout, through a charge sensitive preamplifier, of the signals from the noncollecting grid. When electrons generated by an energy deposit are detected toward the collecting pixel anode near the anode surface, a negative pulse is induced on the noncollecting grid as shown in Figure 10.6c. This signal is differentiated, generating positive pulses corresponding to the slope inversion points of the noncollecting grid signal. Finally, a threshold circuit uses the differential output to provide a logic pulse when it is

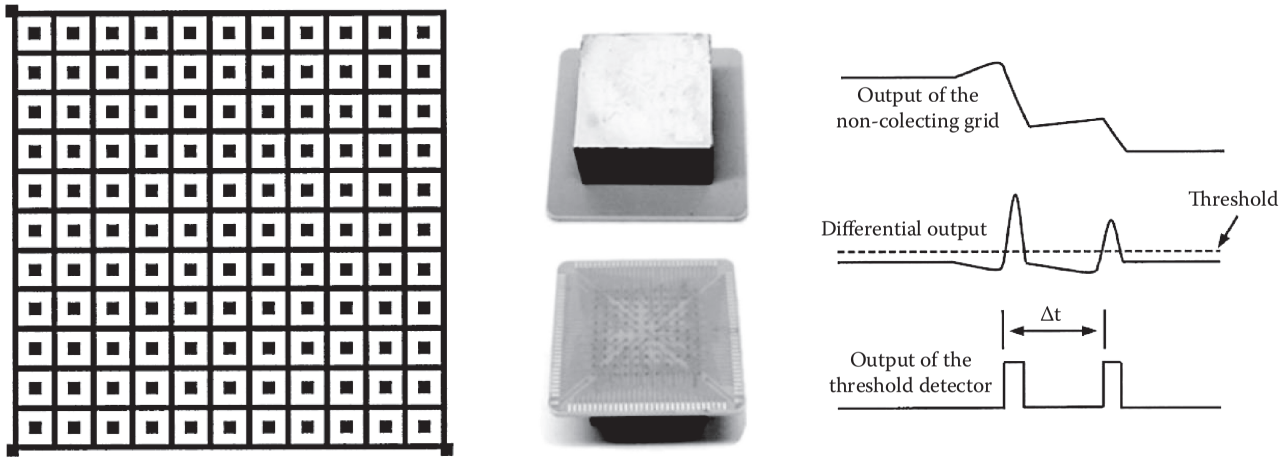

FIGURE 10.6
(a) Scheme of the anode side of the 10×10×10 mm^3 CZT prototype. (Reprinted from *Nuclear Instruments and Methods in Physics Research Section A: Accelerators, Spectrometers, Detectors and Associated Equipment*, 422, 1–3, Z. He,W. Li,G.F. Knoll,D.K. Wehe,J. Berry,C.M. Stahle, 3-D position sensitive CdZnTe gamma-ray spectrometers, 173–178, Copyright 1999, with permission from Elsevier.) (b) Photos of the detector (15 × 15 × 10 mm^3) with the ceramic substrate facing up (top) and with the cathode facing down (bottom), where, through the thin ceramic substrate, the anode bonding pads array is visible. (F. Zhang, Improved resolution for 3-D position sensitive CdZnTe spectrometers, *IEEE Transactions on Nuclear Science*, 51(5), © 2004 IEEE.) (c) Scheme of the depth sensing logic used for multiple-site events handling. (Reprinted from *Nuclear Instruments and Methods in Physics Research Section A: Accelerators, Spectrometers, Detectors and Associated Equipment*, 422, 1–3, Z. He,W. Li,G.F. Knoll,D.K. Wehe,J. Berry,C.M. Stahle, 3-D position sensitive CdZnTe gamma-ray spectrometers, 173–178, Copyright 1999, with permission from Elsevier.)

above a defined threshold (Li et al. 1999). These logic pulses provide start and stop signals to a time-to-amplitude converter (TAC) that measure the electrons drifting time intervals.

By combining the centroid depth, pulse amplitudes from each pixel anode, and the depth interval between energy deposits derived from the measure of electrons drifting time, it is possible to obtain the depth of each hit (Figure 10.7a). Although the differential circuit could identify multiple hits of the same incoming photon, the TAC limits the number of interactions to two. Therefore, the original system was able to provide interaction depths for only single- and two-site (double) events. Events having more than two interactions can be identified using the number of triggered anode pixels, but only the centroid interaction depth can be obtained. While the single event low-energy threshold was small (~10 keV), the threshold for double events results is relatively high, because their detection depends on the noncollecting grid signal threshold being in the first measurements ~100 keV. The reconstructed interaction depth using this technique becomes worse with decreasing energy (Li et al. 2000) and is ~0.25 mm for single events and ~0.4 mm for double ones at 662 keV.

Since the first realization, the same groups have made several improvements on both the CZT sensor configuration and the readout and processing electronics allowing to increase, in particular, the sensitive volume of each CZT device up to 6 cm^3 (i.e., $2 \times 2 \times 1.5$ cm^3) (Zhan et al. 2004, 2012). This sensor can achieve very impressive spectroscopic performance (Figure 10.7b) for all the event types for energy up to several megaelectron volts. One of the main problems operating in this energy regime (>500 keV) is represented by the dimension of the electron cloud, generated at each photon interaction point, that becomes larger than the pixel lateral size (>1 mm) as the energy deposit increases (Figure 10.7c). This effect tends to degrade the spatial resolution because transient signals are collected by several anode pixels around the central one (charge sharing) and, in the direction of charge collection, increase the depth reconstruction uncertainty. The geometrical spatial resolution in the anode plane of the 6 cm^3 sensor was only 1.8 mm. However, with a custom-designed digital readout scheme, handling the charge shared signals out from the eight neighboring pixels of the triggered one, it has been demonstrated that a Δx of 0.23–0.33 (FWHM) mm can be achieved for 662 keV single interaction (Zhu et al. 2011).

Zhu et al. 2011 is not in the reference list. Please provide complete publication details to be added in the reference list or delete citation.

10.3.2 PTF Microstrip with Drift Configuration

Another way to build 3D spectroscopic sensors relies on the use of CZT crystals in the PTF configuration. The drawback of the PTF irradiating geometry is that all the positions between the collecting electrodes are uniformly hit by impinging photons leading to a stronger effect of the difference in charge collection efficiency and then in the spectroscopic performance with respect to the standard irradiation configuration through the

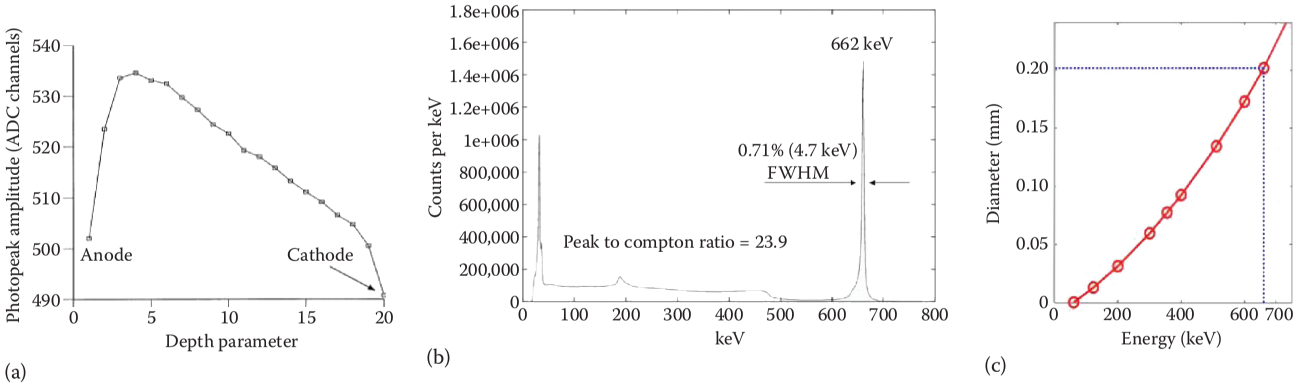

FIGURE 10.7

(a) Typical dependence of the centroids of ^{137}Cs photopeak from the interaction depth parameter (1 depth step = 0.5 mm) for one pixel. (Reprinted from *Nuclear Instruments and Methods in Physics Research Section A: Accelerators, Spectrometers, Detectors and Associated Equipment*, 422, 1–3, Z. He, W. Li, G.F. Knoll, D.K. Wehe, J. Berry, C.M. Stahle, 3-D position sensitive CdZnTe gamma-ray spectrometers, 173–178, Copyright 1999, with permission from Elsevier.) (b) ^{137}Cs Spectrum measured by one pixel after compensation for interaction depth for all event multiplicity. The measured resolution is 0.71% (FWHM). (F. Zhang, Characterization of the H3D ASIC readout system and 6.0 cm^3 3-D Postion Sensitive CdZnTe detectors, *IEEE Transactions on Nuclear Science*, 59(1) © 2012 IEEE.) (c) Diameter of the electron cloud generated by the photon interaction vs energy. (Reprinted from Nuclear Instruments and Methods in Physics Research Section A: Accelerators, Spectrometers, Detectors and Associated Equipment, 654, 1, Kim, J.C. ,Anderson, S.E., Kaye, W., Zhang, F., Zhu, Y., Kaye, S.J. He, Z., Charge sharing in common-grid pixelated CdZnTe detectors, 233–243, Copyright 2011, with permission from Elsevier.)

cathode (PPF). Therefore, worst spectroscopic performances are expected in PTF with respect to standard PPF irradiation configuration (Auricchio et al. 1999). To recover this spectroscopic degradation and to improve the CZT sensitive unit performance, an array of microstrips in a drift configuration can be used instead of a simple planar anode (Figure 10.8): the anode surface is made of a thin collecting anode strip surrounded by guard strips that are biased at decreasing voltages. This anode configuration (Gostilo et al. 2002) allows the detector to become almost a single charge carrier device. This avoids the degradation of the spectroscopic response by the charge loss due to the holes trapping and provides a more uniform spectroscopic response (i.e., independent from the distance of the interaction from the collecting electrodes; Caroli et al. 2010). The spectroscopic resolution of this type of sensor ranges from 6% at 60 keV down to 1.2% at 662 keV, without any correction for the interaction depth. In fact, similarly to the previous configuration presented above, it will be possible to perform a compensation of the collected charge signals using the photon interaction position in between the metalized surfaces that can be inferred by the ratio between the cathode and the anode strip signals (Kuvvetli et al. 2010a).

The achievable spatial resolution in this direction is a function of energy, depending on the dimension of the charge-generated cloud. The measurements have given (Kuvvetli et al. 2010b) a value around 0.2 mm (FWHM) up to 500 keV. Further segmentation of a cathode into an array of metallic strips, in the direction orthogonal to the anode ones, can provide the third hits coordinate, i.e., the 3D sensitivity for the photon interaction position (Figure 10.8c). Of course, with the described configuration, the spatial resolution along the anode surface is defined geometrically by the collecting anode and cathode strip pitch.

Both anode and cathode strips are read out by standard spectroscopic electronics chains, and therefore, the segmentation of cathode and anode surfaces will set the number of readout channels. In fact, ongoing developments on this sensor configuration are demonstrating that with a readout logic able to weight the signal between strips, the achievable spatial resolution along the anode and the cathode strip sets can result finer than the geometrical one. For a CZT sensor, in which the cathode is segmented in 2 mm pitch strips, the final spatial resolution can be as low as 0.6 mm (FWHM, up to 600 keV) weighing the cathode strips signals. In fact, along the anodic strips set, the effective resolution can be further improved to a small fraction (1/5–1/10) of the geometrical pitch between collecting strips by implementing an appropriate readout of the drift strips signal similar to the one suggested by Luke et al. (2000) for 3D coplanar grid detectors (Kuvvetly et al. 2014). This expectation has been confirmed by recent tests on a sensor implementing the PTF drift strip configuration on a $20 \times 20 \times 5$ mm^3 single CZT spectroscopic crystal made at the ESRF (Grenoble) with a fine (50 μm) high-flux collimated monochromatic beam (Figure 10.9). The CZT sensor id characterized by an anode and a cathode pitch of 1.6 and 2 mm, respectively. Using the mentioned

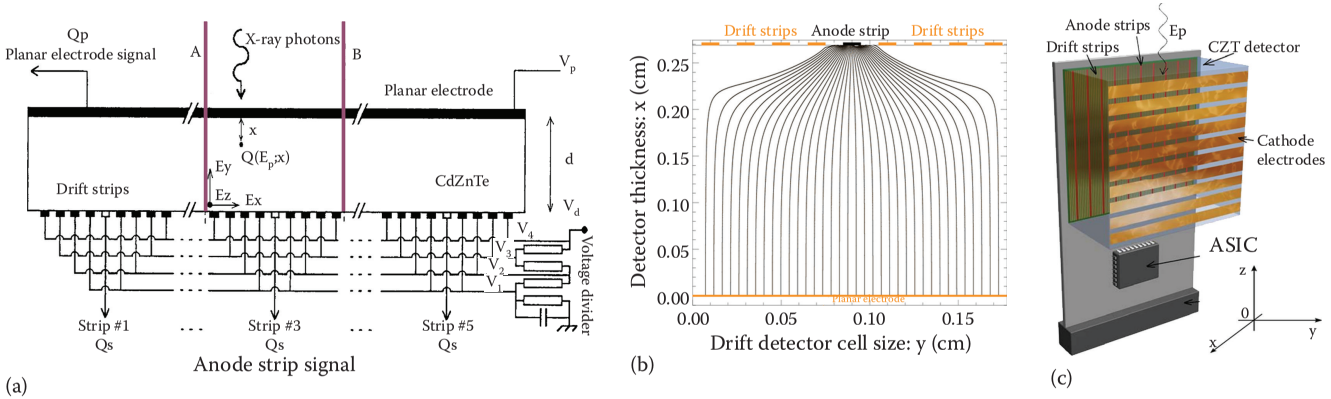

FIGURE 10.8
(a) Schematic configuration of a CZT drift strip sensor. The two thick vertical lines "A" and "B" define the volume of the drift strip cell. The drift strips and the planar electrodes are biased in such a way that the electrons move to the anode collecting strips (central white strips). (b) Shape of the charge collecting electric field calculated for a drift strip cell on a CZT sensor: the anode–cathode bias is set at 150 V, and the difference between each adjacent strip pairs is $\Delta V = -25$ V. (c) Schematic view of a 3D PTF drift strip CZT sensor with segmented cathode.

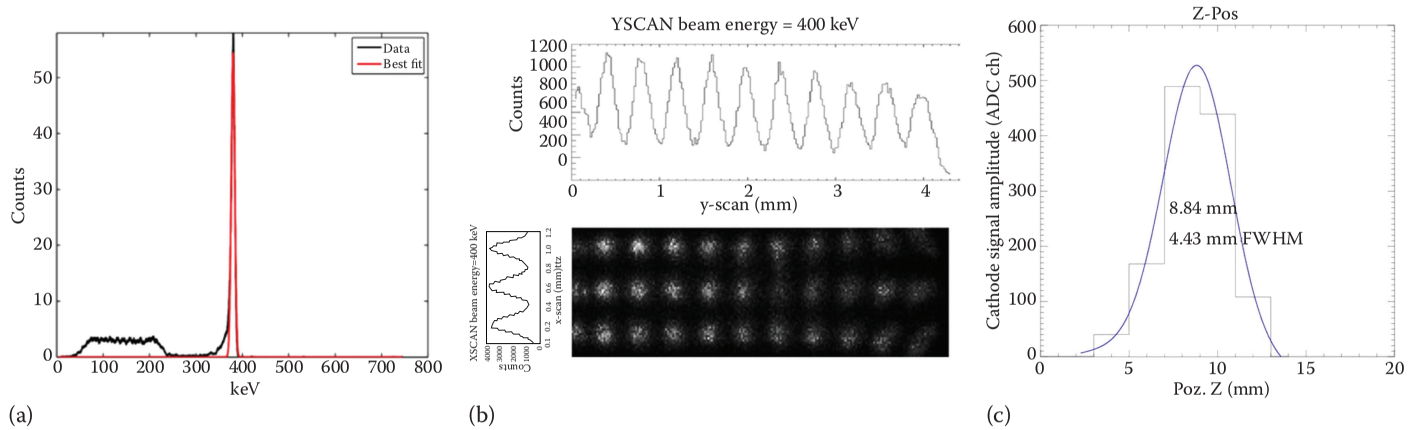

FIGURE 10.9
Performance of a 3D PTF drift strip CZT sensor of 20 × 20 × 5 mm^3 using a fine collimated (0.05 × 0.05 mm^2 spot) x-ray monochromatic beam (ID15A) at ESRF (Grenoble, France). (a) Single events spectrum for 400 keV beam exhibiting an energy resolution of 1.4% (FWHM). (b) Reconstruction of photon (400 keV) interaction position across the impinging surface. The vertical axis is across the anode strips for a total of 1 drift cell (i.e., 1.6 mm), while the horizontal one is parallel to the interelectrode distance (5 mm length). (c) Signal recorded by 10 cathodes for single event, together with the Gaussian fitting giving as resolution for the third coordinate (*z*) 0.45 mm.

technique of drift strips readout and signal weighing, the beam tests have demonstrated very good performance, both in spectroscopy (e.g., 1.4% FWHM @ 400 keV) and in 3D position reconstruction, achieving in all the three directions spatial resolution (FWHM) at a submillimeter level (Δx = 0.15 mm, Δy = 0.26 mm, Δz = 0.65 mm).

Because of the use of the PTF configuration, the dimensions of the 3D sensor unit can reach up to 20–30 mm in the lateral sizes and up to 5 mm as charge collecting distance, allowing one to limit the high-bias voltage required to have a high charge collection efficiency to values below 500 V.

While the electrical field intensity between the cathode and the anode is typically 100 V/mm, the drift strips, to be effective in shaping the charge collection electric field and to minimize dead volume, is biased at decreasing relative voltage with respect to the cathode strips of ΔV = 20–30 V. These values depend, in particular, on the thickness (distance between cathode and anode surfaces) of the sensor tile and the best bias voltage scheme needs to be optimized. Using such PTF CZT drift strip sensor units (Auricchio et al. 2012), large-volume 3D spectrometers can be built by packaging several units as shown in Figure 10.10, in which CZT 3D sensors are bonded on thin high resistivity support layers (e.g., Al_2O_3) forming linear modules that provide the electrical interface both for readout electronics and bias circuits.

A PTF drift strip sensor unit, like the one discussed above, has the great advantage, with respect to pixel spectrometers with coplanar guard grid implementation, represented by the few readout channels (~30) required to obtain a sensor segmentation equivalent to ~8×10^4 "virtual" voxels in a sensitive volume of 2 cm^3. This characteristic is quite important, in particular, for applications with limited power resources, like space astronomy, and opens the possibility to implement efficiently new readout systems based on the use of fast digitizers to record the original charge sensitive preamplifier (Abbene et al. 2015).

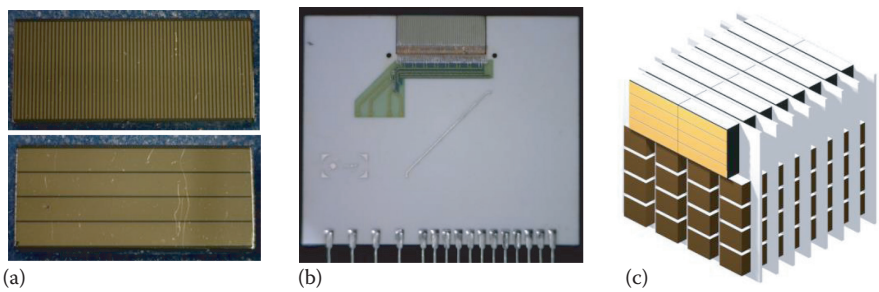

FIGURE 10.10
(a) Drift strip CZT sensor (18 × 8 × 2.5 mm^3): (top) anode side with 64 (0.15 mm wide) strips set; (bottom) cathode side with 4 (2 mm wide) strips set. (b) Linear module prototype seen from anode side: this constitutes the basic element for building a large-volume 3D sensor. (c) Suitable packaging scheme of eight linear modules, each supporting two CZT drift 3D sensors of 20 × 20 × 5 mm^3 to obtain a spectroscopic imager of 32 cm^3 sensitive volume.

10.4 CZT/CdTe Spectro-Imagers for Compton Polarimetry in Astrophysics

High-energy polarized emissions are expected in a wide variety of gamma-ray sources such as pulsars, solar flares, active galactic nuclei, galactic black holes, and gamma-ray bursts (Lei et al. 1997; Bellazzini et al. 2010; McConnell et al. 2009), but polarimetry in this energy regime is still a completely unexplored field mainly due to two facts. In the first place, the expected polarized hard x/γ-rays flux from cosmic sources is, in general, only a small percentage of the already low incoming flux (a few to 10–20%), and only in a few cases can represent a large fraction of it (>40%), requiring very high sensitivity instruments to be detected. Second, x/γ-ray polarimetric measurements require the implementation of the complex of detection, electronic, and signal processing systems, onboard to high-altitude balloon or satellite missions in space. Therefore, until a few years ago, no dedicated hard x/γ-ray polarimetric missions have been launched into space, and x- and γ-ray source emissions have been studied almost exclusively through spectral and timing analysis of the measured fluxes and by using imaging techniques. On the other hand, polarization measurements will increase the number of observational parameters of a γ-ray source by two: the polarization angle and the level of linear polarization. These additional parameters should allow a better discrimination between different emission models characterizing the same object. Polarimetric observations can provide important information about the geometry, the magnetic field, the composition, and the emission mechanisms. In the soft γ-ray domain (0.1–1 MeV), only a few polarimetric measurements were performed by the SPI and IBIS instruments onboard the INTEGRAL (INTErnational Gamma-Ray Astrophysics Laboratory) mission (Winkler et al. 2003; Ubertini et al. 2003), on the Crab Pulsar, on the galactic black-hole Cygnus X-1, and on some high flux gamma-ray bursts (Dean et al. 2008; Forot et al. 2008; Laurent et al. 2011; Götz et al. 2009).

Today, the importance of high-energy polarimetry is largely recognized, and several research groups are involved in the development of dedicated instruments (Kole et al. 2016; Chauvin et al. 2016; Kislat et al. 2017). In any case, the next generation of space telescopes should certainly provide polarimetric observations, contemporaneously with spectroscopy, timing, and imaging. These multipurpose instrument types were proposed in recent high-energy (100 keV–1 GeV) space mission concepts submitted to ESA Cosmic Vision calls where our groups were proposal partners, such as the Gamma-Ray Imager (GRI), DUAL, and e-ASTROGAM (Knödlseder et al. 2007; von Ballmoos et al. 2010; Tatischeff et al. 2016). In the framework of these space mission proposals, different configuration detection planes suitable to high-energy polarimetry are under study and development.

A pixels/voxels detector inherently offers the possibility to operate as a scattering (Compton) polarimeter if equipped with a readout logic that

allows to manage events with two (double events) or more (multiple events) interactions in coincidence (Figure 10.11a). Furthermore, a polarimeter based on a pixel/voxel detector permits an optimal use of the entire sensitive volume, since each element operates in the same time as a scatterer and as an absorber one. Another important advantage for the use of segmented detectors, such as 2D/3D spectro-imager as a Compton polarimeter, is to allow the use of the same detector to make contemporary spectroscopy, timing, and imaging measurements. This capability allows overcoming problems linked to the inherent time variability of both cosmic sources flux and instrumental background, making it possible to directly correlate the various types of measurement for the same observation.

The choice of CZT/CdTe spectroscopic imager as a scattering polarimeter, mainly to optimize the detection efficiency, for the high Z of the material, and simultaneously ensure good spectroscopic performance and high spatial resolution (2D or 3D), obviously implies a limitation on the low-energy threshold useful for polarimetric measurement. As in these materials, the Compton cross section becomes significant only above 100 keV; by equating the photoelectric one approximately at 200 keV, CZT/CdTe spectro-imagers can work efficiently as scattering polarimeters above 100 keV and depending on the thickness up to energies of a few megaelectron volts.

10.4.1 Compton (or Scattering) Polarimetry Principle

The polarimetric performance of a high-energy detection plane is determined by the fundamental concepts associated with polarized Compton interactions and by its design. The Compton scattering of a polarized photon beam generates non-uniformity in the azimuthal angular distribution of the scattered photons. The scattered photon's angular direction depends on its initial polarization angle. If the scattered photon goes through a new interaction inside the detector, the statistical distribution of the photon's angular directions defined by the two interactions (double event) provides a modulation curve from which the degree and polarization direction of the incident beam can be derived. The angular distribution of the scattered photons is given by the Klein–Nishina differential cross section for linearly polarized photons:

$$\frac{d\sigma}{d\Omega} = r_0^2 \left(\frac{E'}{E} \right)^2 \left[\frac{E'}{E} + \frac{E}{E'} - 2 \sin^2 \theta \cos^2 \phi \right] \tag{10.3}$$

where r_0 is the classical electron radius, E and E' are, respectively, the energies of the incoming and outgoing photons, θ is the angle of the scattered photons, and ϕ is the angle between the scattering plane (defined by the incoming and outgoing photon directions) and the incident polarization plane (defined by the polarization direction and the direction of the incoming photon). As can

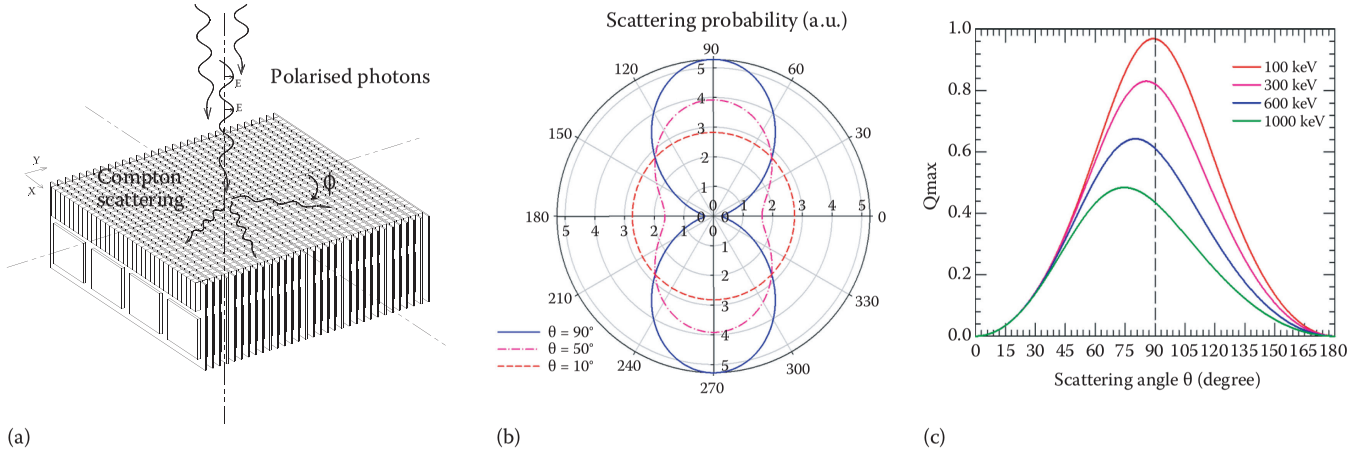

FIGURE 10.11
(a) Scheme of a CZT pixel detector used as a scattering polarimeter. The polarization vector direction is along the *y*-axis. (b) Azimuthal angle (ϕ) probability distribution for a given Compton scattering angle (θ) of linearly polarized photons at E = 200 keV derived from Equation 10.3. The direction of the polarization is parallel to the horizontal axis of the polar plot. The probability distribution of the scattering angle will present a maximum along the orthogonal direction to the polarization plane and a minimum in the parallel direction. (c) Maximum modulation expected (Q_{max}) as a function of the scattering angle for different impinging photon energy.

be seen from Equation 10.3, after fixing all the other parameters, the scattering probability varies with the azimuthal angle ϕ and its maximum and minimum arises for orthogonal directions (Figure 10.11b). For ϕ = 0°, the cross section reaches a minimum and for ϕ = 90°, the cross section reaches a maximum. However, this relative difference reaches a maximum for a scattering angle θ_M, dependent on the incident photon energy (Lei et al. 1997). For hard x/γ-rays (0.1–1 MeV), the θ_M value is 90° at 100 keV slowly decreasing down to ~75° at 1 MeV (Figure 10.11c). Note that E and E' are related through

$$\frac{E'}{E} = \frac{1}{1 + \frac{E}{m_0 c^2}(1 - \cos\theta)} \tag{10.4}$$

where c is the speed of light in free space, and m_o is the electron rest mass.

The modulation factor, Q_{100}, of double-event distribution generated by a 100% polarized beam provides the evaluation of the polarimetric performance of an instrument. For the case of a planar pixelated detector, Q_{100} can be calculated from the modulation curve resulting from a double-event angular distribution around a central irradiated pixel:

$$Q_{100} = \frac{N_{\parallel} - N_{\perp}}{N_{\parallel} + N_{\perp}} \tag{10.5}$$

where $N_{\parallel}$ and $N_{\perp}$ are the double events integrated over two orthogonal directions defined on the detector plane along the maxima and minima of the modulation curve (Suffert et al. 1959).

For a given polarimeter, another parameter is of fundamental importance to quantify its final performance, once implemented in a particular instrument: the minimum detectable polarization (i.e., MDP). MDP indicates when one may be confident that polarization is detected, i.e., that the source is not unpolarized. The expected MDP should be significantly smaller than the degree of polarization to be measured. For a space polarimeter in a background noise environment, the following relation estimates the MDP at 99% (3σ significance) confidence level (Weisskopf et al. 2009):

$$MDP_{99\%} = \frac{4.29}{A \cdot \varepsilon \cdot S_F \cdot Q_{100}} \sqrt{\frac{A \cdot \varepsilon \cdot S_F + B}{\Delta T}} \tag{10.6}$$

where Q_{100} is the modulation factor for a 100% polarized source, ε is the double-event detection efficiency, A is the polarimeter detection area in cm^2, S_F is the source flux (photons s^{-1} cm^{-2}), B is the background count rate (counts/s), and ΔT is the observation time in seconds.

10.4.2 Polarimetry Modulation in CdTe/CZT Pixel Spectrometers

To optimize the polarimetric performances of future high-energy space proposals, a series of experiments based on CZT/CdTe pixel detector prototypes were carried out at the European Synchrotron Radiation Facility (ESRF), where a ~99% polarized gamma-ray beam is available (Curado da Silva et al. 2004, 2008, 2011, 2012; Caroli et al. 2009; Antier et al. 2015). The main purpose of these experiments, denominated as POLCA (POlarimtery with Cadmium Telluride Arrays) series, was to assess the performance of a CZT/CdTe focal plane as a polarimeter up to 750 keV. Monte Carlo simulations were also performed, implementing in the code the same CZT/CdTe detector prototype design irradiated under analogous conditions. The Monte Carlo simulation code was based on the GEANT4 (GEometry ANd Tracking, Allison et al. 2016) a very suitable and efficient tool. The simulation code implemented two main functions: (a) the modules implementing the physics of the electromagnetic interactions of polarized photons, in particular, for the Compton scattering; and (b) the detection system with the definition of the beam characteristics, the detection plane design (geometry and material), and the readout logic.

The POLCA experimental system was composed of four functional subsystems: the synchrotron beamline optical system, the CdZnTe detection system (Figure 10.12), the shaping and coincidence electronic system, and the control and data acquisition workstation.

10.4.2.1 Synchrotron Beamline Optical System

The ID 15A beamline optical system allows tuning the energy of the monochromatic photon beam between 100 keV and up to 1 MeV, with a beam spot

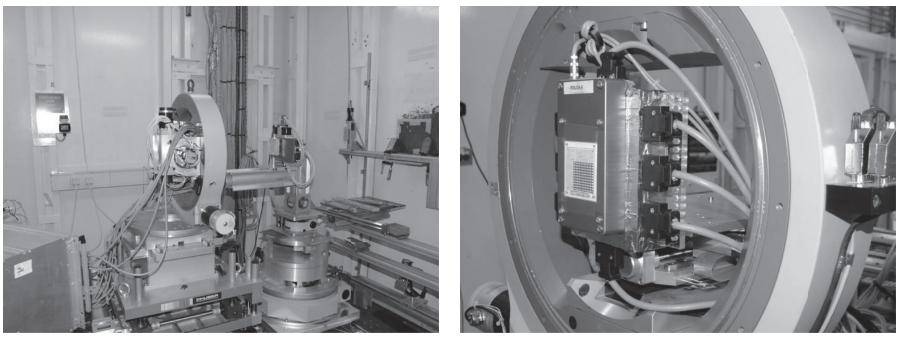

(a) (b)

FIGURE 10.12
(a) Setup inside the experimental hutch of the ID15A beamline at the ESRF. The large ring provides the rotation around directions parallel to the beam axis. (b) In its center, the CZT pixelized prototype detector system is visible with its readout cables.

of about 500 μm in diameter and a linearly polarized component at the beam center higher than 99% (ESRF 2017).

10.4.2.2 CdZnTe Detection System

Several types of CZT/CdTe detectors (Eurorad, IMARAD, and ACRORAD) were tested under POLCA experiments. Herein, we concentrate on the results obtained with the most tested model during these experiments: the IMARAD detector. This polarimeter prototype was based on an IMARAD 5 mm thick CZT mosaic of four units with anodes segmented to obtain a total of 16×16 pixels, each with 2.5 × 2.5 mm^2 area. Due to limitations in our back-end electronics (only 128 channels available), only 11 × 11 pixels have been connected for a total sensitive area of ~8 cm^2. The CZT unit was installed on a supporting layer that contains the readout application-specific integrated circuit (ASIC) supplied by eV Products, Pennsylvania, USA (De Geronimo et al. 2003), the bias circuit, and the connectors for the back-end electronics (Figure 10.12b). The device sensitivity is determined from the energy selectable from 1.2 to 7.2 mV/keV and a peaking time variable between 0.6 and 4 μs.

10.4.2.3 Shaping and Coincidence Electronic Subsystems

The signals were processed by a custom multiparametric system consisting of 128 independent channels with filters, coincidence logic, and analog-to-digital converter (ADC) units (Guazzoni et al. 1991). When operating in coincidence mode, all signals exceeding the lower energy threshold occurring in the same coincidence time window (2 μs) are analyzed as generated by the same event. The typical irradiated pixel count rate was about 10^4 counts/s.

10.4.2.4 Data Acquisition Unit

This unit was based on a commercial data acquisition card PXI DAQ-6533 provided by National Instruments connected to a personal computer and controlled by a LabView application. For each event, we obtained information about the number of hits, the triggered pixels, and the energy deposited in each hit (Caroli et al. 2002). The recorded data are analyzed offline by an *interactive data language* (IDL 2017) s/w custom tool, which allows the selection of single, double, and multiple events (photons undergoing at least three interactions in the detection plane).

The CZT prototype was tested under a 500 μm diameter monochromatic linearly polarized beam from 150 up to 750 keV in steps of 100 keV. The experimental procedure adopted in order to minimize several factors that might introduce errors in the calculation of Q, such as the non-uniformity of the detection efficiency of the pixels that compose the 11×11 CZT matrix

and the misalignment of the beam with respect to the irradiated pixel center, consisted of four steps for each energy:

1. The photon beam was aligned with respect to four pixels (2×2) by displacing the mechanical system until the number of events in the four pixels became almost uniform. This identified the centroid of the 2×2 pixels.
2. The beam was aligned with the center of each pixel in turn, because our beam had a maximum spot diameter of 500 μm, and a slight deviation from this position could be responsible for an undesirable artificial asymmetric distribution due to a different mean free path for scattered photon in the neighboring pixels.
3. Each of the 11×11 CdZnTe pixels was irradiated by the polarized beam by moving the detector in the x and y directions with 2.5 mm steps.
4. The detector was rotated by 90° with respect to its initial position and the steps from 1 to 3 were repeated in order to confirm the 90° double-event scattering distribution symmetry.

The single events obtained in each of the directly irradiated pixels allowed us to determine the relative detection efficiency map of the 11×11 pixels. The data were used to perform the correction of the non-uniformities in the response of the CZT detector pixels. The true double-event counts N_{true} for each pixel becomes

$$N_{true} = \frac{N_{pol}}{N_{non}} N_{\max} \tag{10.7}$$

where N_{pol} is the number of double events detected (that depend on the beam polarization), N_{non} is the number of single events of the response map obtained when the pixel is directly irradiated, and N_{max} is the maximum value among all the matrix pixels N_{non} (Lei et al. 1997). By applying this method to the pixels around the irradiated pixel, the error introduced by the non-uniformity of the detector matrix response is minimized, and the double-event distributions obtained allow improving the precision of the modulation Q factor of the CZT prototype, which is given by Equation 10.5.

Figure 10.13 shows false color maps resulting from double-event distributions generated by a 511 keV monochromatic beam with polarization angles of 0° and 45°. As can be seen, double events are not uniformly distributed around the irradiated pixel for a polarization angle of 0°. As expected from theory, a maximum number of Compton photons were detected in the pixels along the direction defined by the top–center–bottom of the matrix. Polarization direction is perpendicular to the maximum intensity direction,

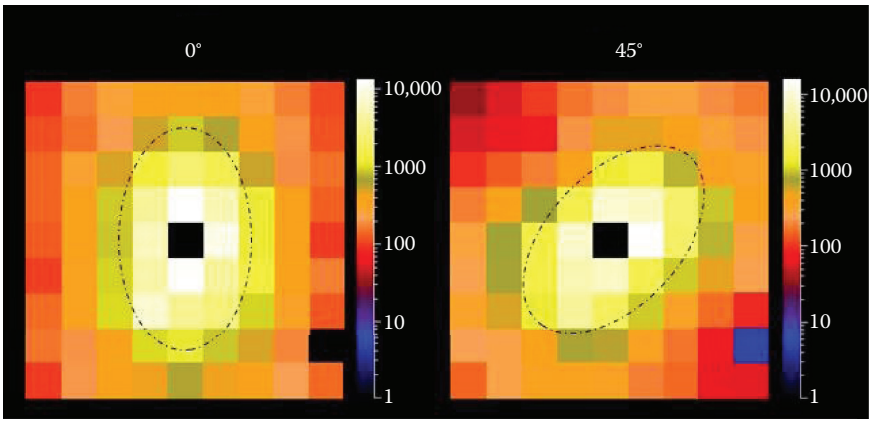

FIGURE 10.13
Double-event maps obtained for a 100% polarized beam at 500 keV by rotating the polarization by an angle φ of 0° and 45°. The 500 keV beam was directed to a CZT matrix central pixel, in black at the center. The dashed ellipse superposed at the center of each double-event distribution is represented to guide the visualization of polarization angle rotation over the matrix. Note that the major ellipse axis is oriented with the pixels along the direction where higher numbers of Compton photons were recorded. The minor axis is perpendicular and is aligned with the incoming beam polarization direction.

represented by the major axis of the ellipse (represented only for guideline purposes) superposed to the double-event distribution. Auxiliary ellipse minor axis takes the incoming polarization direction. When the CZT matrix is rotated by 45°, the projection of the polarization in the detector plane is also rotated by the same amount. It is noticeable in Figure 10.13 that the direction traced by the ellipse's major and minor axis rotates according to the polarization angle apparent rotation.

Figure 10.14a shows the modulation factor Q calculated for the CdZnTe prototype as a function of the polarized photon beam energy. These values were obtained after the correction for the non-uniformity in the response of the detector throughout its pixelated volume by using the method explained above where *true* double events are given by Equation 10.7. For comparison, Monte Carlo simulations were performed with a 5 mm thick CdZnTe matrix similar to the POLCA prototype under analogous conditions. The modulation factor Q values obtained from these simulations are shown in Figure 10.14.

The experimental modulation factor Q obtained is about 0.35 or higher up to 350 keV. It decreases to about 0.15 for 650 keV, since for higher energies the probability of Compton interactions occurring with a scattering angle θ lower than 90° is higher than in the 150–350 keV band. Lower scattering angles provide poorer polarization information; the optimum scattering angle θ_M is about 90° for soft gamma-rays and hard x-rays. Furthermore, a lower θ also means that a higher fraction of Compton scattered photons escape the CdZnTe without interacting a second time in the crystal. The fraction of photons that

cross the CdZnTe matrix without interaction also increases with the beam energy. As can be seen in Figure 10.14, the CdZnTe prototype performances obtained up to 450 keV are in good agreement with the Monte Carlo simulation results performed with a GEANT4-based code. From 550 keV to higher energies, a secondary synchrotron beam (due to a gap in the beam collimator

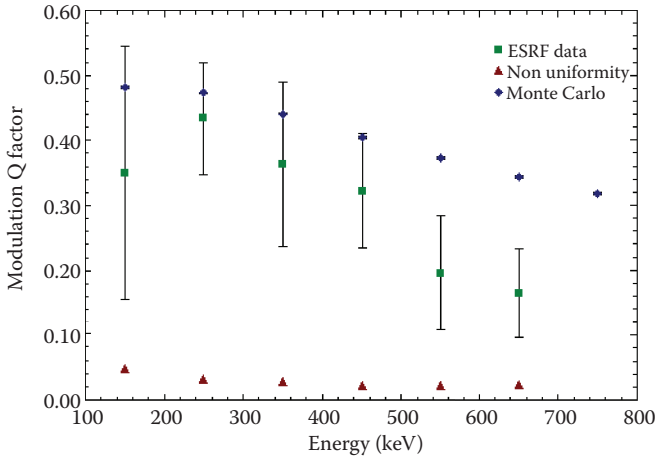

(a)

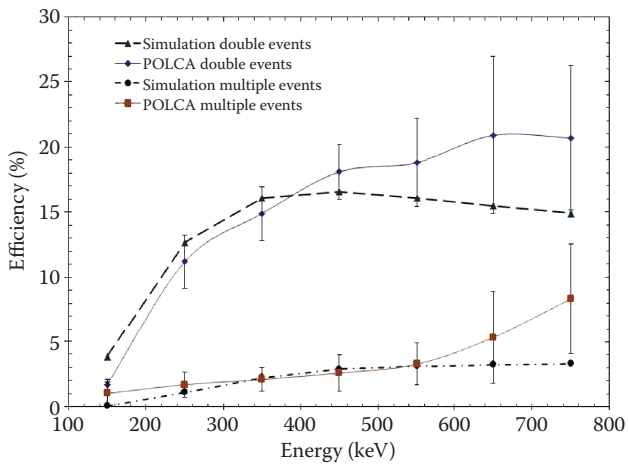

(b)

FIGURE 10.14
(a) *Q* factor as a function of the energy for a 5 mm CdZnTe prototype when irradiated by a monochromatic ~99% polarized photon beam. Monte Carlo simulation results obtained in similar conditions are shown for comparison. The modulation generated by the non-uniformity of matrix pixels response is also represented (triangle). The simulated residual modulation obtained for an unpolarized beam in the same energy range was lower than 0.01 [8]. (b) Experimental and Monte Carlo double and multiple events' relative efficiencies (double events/total detected photons and multiple events/total detected photons) as a function of the γ-ray beam energy.

shield) was projected onto the CdZnTe active surface area, which introduced a substantial error component in the Q factor calculation. For 750 keV, the secondary was so dramatically close to the main beam (a few pixels) that the double-event distributions of the two beams overlapped, and it was not possible to perform the polarimetric analysis of our prototype.

The double and multiple events' relative efficiencies (double events/detected photons and multiple events/detected photons) obtained over the experiment energy range are shown in Figure 10.14b together with efficiencies obtained from Monte Carlo simulations. The absolute efficiency (events/incident photons) was not determined since the auxiliary instruments of the ID 15 beamline were not stable and did not accurately measure the count rate of the photon beam. As can be seen in Figure 10.14b, up to 550 keV, the double-event relative efficiency increases with the energy in agreement with the Monte Carlo data, up to about 18%. However, from 550 keV up, experimental efficiency values diverge from the Monte Carlo relative efficiencies, attaining about 20% for 750 keV, while Monte Carlo simulations show a slight diminution of the efficiency for higher energies. Since Compton scattering probability increases with energy, the double events detected increase up to 550 keV, and then lower Compton scattering angles favor escape Compton photons that leave the CdZnTe block without undergoing a second interaction, which explains why the efficiency decreases slightly as the beam energy is increased. The experimental divergence for higher energies is explained by the difficulty to exclude coincidence events generated by the simultaneous projection of the main and secondary beams in the detection plane that occurred from 550 keV up. The multiple-event efficiency increases with energy, since the original photon energy becomes sufficiently high in order to increase noticeably the probability to generate two successive Compton scatterings. However, comparison between Monte Carlo generated and experimental multiple-event relative efficiencies shows similar divergence to the double-event curve, confirming that simultaneous beam detection in the CdZnTe plane artificially increases the efficiency of events measured in coincidence. This problem could be solved if the distance between the detector and the beam output window is increased. Unfortunately, the rack where the mechanical system was mounted was already at its maximum distance from the beam window. Excluding this anomaly for higher energies due to multiple beam detection, both experimental relative efficiency results are in good agreement with the results obtained by the Monte Carlo simulation code.

10.4.3 Polarimetry Optimization of CdTe/CZT Pixel Detector

In order to optimize a CdZnTe focal plane for γ-ray polarimetry in astrophysics, we tested several CZT/CdTe pixel prototypes in a series of experiments covering various aspects, from polarimetric performance to possible sources of systematic error. Several factors limit the performance of a polarimeter

when measurements take place under conditions that are not ideal. One of the most important is the angle between the polarimeter detection plane and the direction of the incoming polarized photons. If the direction of the incoming photons is not orthogonal with respect to the detector plane, the observed modulation of the Compton events distribution is distorted. The degradation of polarimetric measurements will be more important as the angle of the off-axis source increases. The optical system employed to collect photons will influence the direction of the incoming photons. In the case of coded mask telescope, the tilt angle is the same for all photons from one source, but when Laue lenses are used, photons are diffracted at different angles, but typically at less than 1° tilt angle with respect to the optical axis. The effect of impinging photon beam inclination on the measured polarization is also dependent on the pixel size, because this characteristic influences the separation of the hits in a scattered event. Therefore, it is important to determine the maximum tilt angle for which the real polarization modulation is only faintly affected. Another important factor is how the polarimetric sensitivity of the detector depends on the polarization level of beam polarization (i.e., the minimum percentage of polarized photons that the detector is able to detect), since its configuration (mainly spatial resolution and geometry) might limit the capacity to recognize a weakly polarized source. Because of the "square" geometry of scattering elements in a typical pixel detector, systematic effects are introduced in the polarimetric modulation when the incident polarization plane angle is not parallel to one of the detector pixel sides. In fact, square pixels introduce a quantization effect in the distribution of the polarized scattered photons that limits the angular resolution of the polarimeter when considering pixels at different distances from that which scattered the incoming photon. Herein we extend this investigation, obtaining a finer response to the polarization angle direction, not only testing the detector response to a wider set of angles, but also by carefully choosing angles that are not redundant when considering the matrix double-event distribution. The double-event spread pattern in a square pixel matrix repeats itself every 45° (10° is equivalent to 80°, 20° to 70°, 30° to 60°, etc.); therefore, we tested our polarimeter in a 0° to 45° angle range at 5°, 10°, 20°, 30°, 40°, and 45°.

Firstly, the CZT detector central pixel was irradiated by a polarized beam forming different inclination angles with the optical detector axis: 0°, 0.5°, 1°, 1.5°, 2°, 3°, 4°, 5°, and 10°. These measurements at different tilt angles were repeated for different energies (200, 300, 400, and 511 keV) and for polarization vector directions parallel to both the detector plane axis: x and y. Then the modulation factor Q as a function of the inclination angle Θ was calculated from the double-event distributions obtained from each measurement.

Figure 10.15a shows the Q factors as a function of the tilt angle. Up to 2° tilt angle, the Q factor is not significantly affected by the beam inclination. However, from 3° up to 10° tilt angles, the Q factor dramatically increases when polarization and inclination add their effects and decreases when these effects partially cancel each other. These results confirm previous simulation

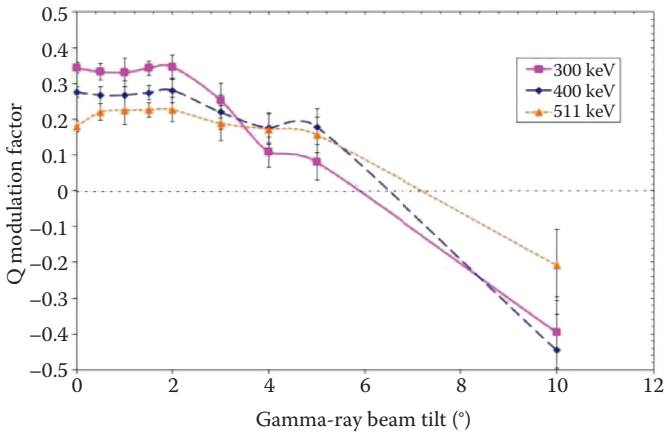

(a)

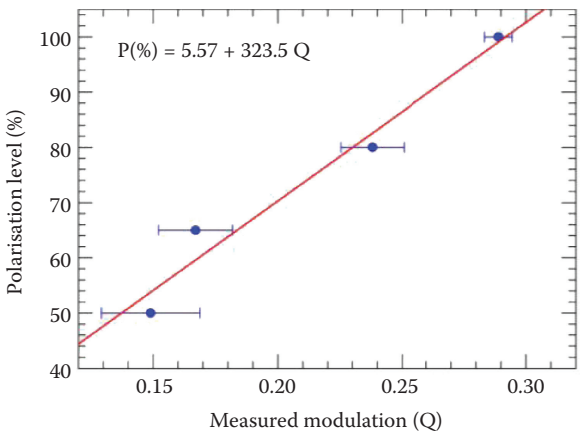

(b)

FIGURE 10.15
(a) The modulation factor *Q* as a function of the tilt angle of the ESRF 100% polarized beam for different energies. In these measurements, the polarization vector was parallel to the *x*-axis. (b) Measured factor *Q* as a function of the polarization level from 100% to 50% of a 400 keV photon beam. The error associated to each point was obtained by averaging the measured *Q* for a set of measurements at the same beam polarization level. These results show a good linearity of the polarimetric response of the used CZT pixel detector to the levels of the γ-ray beam polarization.

studies performed by a Monte Carlo simulation program based on GEANT4 (Curado da Silva et al. 2003). Both experimental and simulation results show that during an observation period onboard a γ-ray satellite, it is essential that polarized sources are no more than 2° off-axis in order that polarization measurements are not affected. This study shows the importance of a pointing system with accuracy better than 1° for an instrument designed for polarimetry. This accuracy should be sufficient so that double-event distributions can be read directly without further data correction methods.

Afterward, the polarimetric sensitivity of a CZT prototype, as a function of the polarization fraction of the incoming γ-ray beam, was tested. Tests were limited to one energy because of time limitations resulting from the very low flux at lower polarization degrees. During each measurement, a polarized 400 keV monochromatic beam irradiated one of the four central pixels of the CZT matrix. The polarization angle was fixed in a parallel direction to the detector *x*-axis. Measurements were performed for different beam polarization degrees: 100%, 80%, 65%, and 50%. The measurement live time was tuned to acquire, in the pixels situated near the irradiated one, a number of double events of the order of 10^4, so that a good polarimetric sensitivity could still be achieved.

The modulation factor *Q* was calculated from the double-event distributions generated by each measurement performed at different beam polarization degrees. The fraction of double and multiple events recorded by the detector was ~20% and ~3%, respectively (Curado da Silva et al. 2004, 2008). Multiple events do not enter into our calculations since the data handling system cannot determine the order of each hit. For double events, we know which is the first interaction because this is coincident with the position of the pixel irradiated by the collimated beam. Therefore, during the analysis, we exclude double events that do not have at least one interaction in the target pixel, e.g., chance coincidence events due to noise and flaring pixels and/or triple events in which the first interaction in the target pixel was under the low-energy threshold (~30 keV). Furthermore, because the impinging beam was monochromatic, we applied a further simple selection of double events using the energy deposited in each hit. Knowing the beam energy, we have selected as good double events only those in which the sum of the two interactions is within a window centered at the selected beam energy within 3σ derived from the expected energy resolution at that energy—evaluated by a simple square root relation derived from calibration data with radioactive sources. Energy resolution (FWHM) ranged between ~8% and 7% for single events and between 16% and 15% for double events in the 200–400 keV band. Although energy resolution was relatively high, this was not a critical factor for polarization performance analysis in the adopted experimental setup.

Figure 10.15b shows a good linear relation between the polarization level of the beam and the measured factor *Q*. At least, down to 50%, this CZT prototype exhibits a good sensitivity to the beam polarization degree. The error associated to each point of Figure 10.15b was obtained by averaging the *Q* values for a set of measurements at the same beam polarization degree. Previous measurements revealed a background noise residual factor *Q* of about 0.02 (Curado da Silva et al. 2011) that would limit our polarimetric sensitivity in the described experimental conditions (setup and acquisition time and CZT pixel detector configuration) to about 12% when extrapolating the linear fitting.

In order to evaluate the accuracy of the polarization angle measurement of a planar CZT matrix prototype, additional tests were performed using

the ESRF ID15 beamline. A central pixel was irradiated by a 100% polarized monochromatic beam at different energies (200, 300, 400, and 511 keV), and the support ring of the detector prototype was rotated by an azimuthal angle φ of 5°, 10°, 20°, 30°, 40°, and 45° (Figure 10.16a). It is relevant to choose a set of nonsymmetrical angles relative to 45° when testing a square pixel matrix; otherwise, double events generate similar distributions. As mentioned before, in previous experiments, other authors tested square matrices rotating the polarization angle only by 30° and 60° (Xu et al. 2005)—angles whose double-event distribution is going to spread in a symmetrical pattern throughout the whole array—and by 45° (Kroeger et al. 1996).

Figure 10.16b shows the measured polarization angle (φ_{obs}) as a function of the effective ESRF beam polarization angle (φ_{beam}) at 200, 300, 400, and 511 keV. The linear fits calculated for each energy are also represented. Overall analysis of these results shows a good agreement between measured polarization angle and the effective beam polarization angle. The error bars of most of the measured polarization angles lie within a few degrees.

The best agreement between φ_{obs} and φ_{beam} was found for the set of measurements performed at 300 keV. Actually, it is at approximately 300 keV that better polarization sensitivity is obtained ($Q \sim 0.4$), as shown in a previous study performed with the same CZT prototype and at the same beamline (Curado da Silva 2008). Furthermore, errors associated with polarization angle observations show that systematic effects due to the square pixels generate higher uncertainties for angles near 45°. This is an expected result, since for these angles, the pixels that correspond to the maximum and minimum directions of the double-event distribution lie close to the diagonal of the detector plane axis, where the effect due to square pixels is more pronounced. When square pixels or parallelepiped voxels are the only technical solutions available, another way to minimize this problem consists of employing pixels of shorter lateral size, improving the spatial (and angular) resolution of the double-event distribution, and therefore reducing the systematic effects.

In order to study the optimal pixel size of the Laue lens telescope focal plane, the MDP was calculated as a function of pixel lateral size dimensions under the same irradiation conditions as explained before. Since the expected point spread function is of about 30 mm, a pixel scale of a few millimeters (1–3 mm) would be enough to have a good sampling from the imaging and source detection point of view. A smaller pixel scale would allow a better sensitivity to the polarized emission, but it means an increase in the focal plane complexity (a large number of channels require more complex electronics and more resources). Therefore, we limited our study to pixel lateral dimensions between 0.5 and 2 mm. Figure 10.16c shows the factor Q and the MDP (for 10^6 s observation time) obtained for a broad band Laue Lens in the 120 to 200 keV energy band-pass combined with a 10 mm thickness CdTe focal plane. Since a 32×32 CdTe matrix is constantly simulated, for lateral pixel sizes smaller than 1.0 mm, its volume is smaller and therefore a fraction

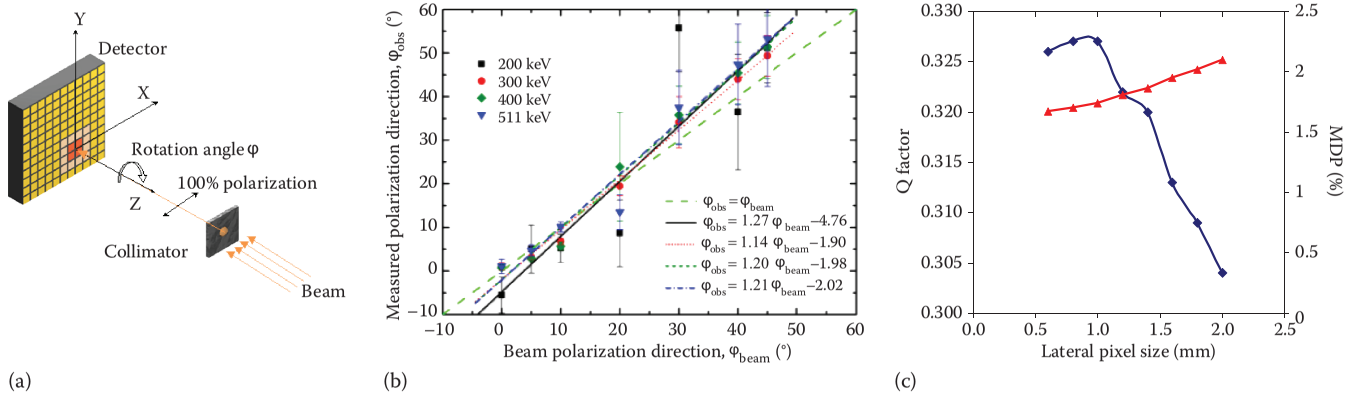

FIGURE 10.16
(a) Schematic view of the experimental setup. The beam polarization is represented at 0°, horizontally oriented relative to the experimental hutch reference frame. The detector was rotated around the beam axis (*z*-axis) by different angles to obtain polarization orientations, which are not parallel to the detector axis, as expected when observing a cosmic source. (b) Measured polarization angle (φ_{obs}) as a function of the effective ESRF beam polarization angle (φ_{beam}) for different energies. The errors associated to each measured polarization angle were obtained by averaging the angle of the two maxima and the two minima of each double-event modulation curve applying a 90° independent partial fitting, since the polarization is 90° symmetric. A linear fitting was applied for each energy. (c) Factor *Q* (diamonds) and the MDP (triangles) for a 10^6 s observation time as a function of pixel lateral size obtained for a broad band Laue lens with a 10 mm thick CdTe focal plane in the 120–200 keV energy band.

of Compton photons escape from the detection plane before having a second interaction, which explains why Q decreases for lateral sizes smaller than 1.0 mm. From 1.0 mm up, this effect becomes residual and smaller lateral dimensions result in higher factor Q values due to a higher rate of second interactions occurring inside pixels further from the central pixel, which contributes to an improvement in the double-event distribution angular resolution. However, the net gain observed in the MDP for pixel dimensions lower than 1 mm does not compensate for the technical difficulties associated with its production. Therefore, focal plane pixel lateral dimensions of about 1 up to 2 mm provide a good trade-off between focal plane complexity and polarimetric performance. Furthermore, we point out that the improvement in the MDP achievable with the smaller pixel scale might be obtained with less expensive background noise reduction techniques such as optimizing the shielding and/or applying event selection procedures based on Compton kinematics.

10.5 Consideration on CZT/CdTe Spectroscopic-Imager Applications and Perspective for Scattering Polarimetry

The development of CZT/CdTe spectrometers with high 2D/3D spatial resolution and fine spectroscopy represents a challenge to the realization of a new class of high-performance instruments, for hard x/γ-rays, able to fulfill the current and future requirements in several applications fields.

Such detectors can achieve very good detection efficiency at high energy (up to a few megaelectron volts; Boucher et al. 2011), without significant loss of spectroscopic performance and response uniformity. These characteristics, together with room-temperature operability, are appealing for application in radiation monitoring and identification (Wahl and He 2011), in industrial noninvasive controls, in nuclear medicine, and in hard x/γ-ray astronomy instrumentations.

Furthermore, 3D CZT/CdTe spectro-imagers, because of the fine spectroscopy (few % at 60 keV and <1% above 600 keV) and the high 3D spatial resolution (0.2–0.5 FWHM mm) achievable, allow operation not only in full energy mode but also as Compton scattering detectors if equipped with appropriate electronics providing a suitable coincidence logic to handle multihit events. These possibilities imply that these sensors are suitable to realize wide field detector for γ-ray sources (>100 keV) localization and detection both in ground and space applications (Xu et al. 2004). Evaluation done using a single thick 3D CZT sensor (Section 10.3.1) as a 4π Compton imager has demonstrated the possibility to obtain an angular resolution

~15° (FWHM) at 662 keV. This is really an excellent result in the small distance scale used to reconstruct the Compton events kinematics and can be achieved only because the good 3D and spectroscopic performance of the CZT proposed sensor units.

As seen in Section 10.4, the possibility operating 2D/3D CZT/CdTe spectrometers as Compton scattering detectors relies on the appealing opportunity to use these devices for hard x/γ-rays polarimetry. Today, this type of measurement is recognized for its fundamental importance in high-energy astrophysics and is one of the most demanding requirements for next space mission instrumentation in this energy band (10–1000 keV). This capability is well described in Section 10.4 by using both the experimental results and Monte Carlo evaluations obtained by authors for 2D CZT/CdTe pixel detector (2D spectro-imager).

In fact, a 3D spectrometer able to handle properly scattered events in three dimensions over the entire sensitive volume can offer even better performance as a scattering polarimeter. In the case of 3D spectrometer devices, such as described in Section 10.3.3, each single sensor unit could be operated as a Compton polarimeter (Xu et al. 2005). The quality (modulation factor) of a scattering polarimeter strictly depends on both spatial and spectroscopic resolution, because these characteristics affect the capability of Compton kinematic reconstruction and good event selection (Curado da Silva et al. 2011; Antier et al. 2015).

The development of 3D CZT/CdTe spectroscopic imagers in the coming years represents a great opportunity for the implementation of high-performance detectors operated as high-efficiency scattering polarimeters. This development can definitely open the polarimetric dimension in hard x/γ-rays astronomy, making polarimetry the new standard observation mode in the next space instrumentation. Compared to the pixel detectors, the determination of the 3D position of each hit in scattering events represents a great advantage in the measurement of polarization as it allows a more accurate reconstruction of the Compton kinematics and therefore a more efficient selection of the events to optimize the response to the polarization modulation. For example, a better Compton kinematic reconstruction allows implementing reliable methods to recognize good events (i.e., events form the source) with respect to chance coincidence ones and background events, improving the signal-to-noise ratio of the detection. The 3D spatial resolution capability can help also to handle some typical systematics that can negatively affect polarization measurements, like the one introduced by incoming flux direction angle (Section 10.4.3). Furthermore, the possibility to select events within thin layers of the sensitive volume, thanks to the 3D segmentation of the detector, (i.e., close to 90° scattering direction), improves the modulation factor and therefore the reliability of the polarimetric measurements (Caroli et al. 2015).

References

Abbene, L. et al. (2007), "Spectroscopic response of a CdZnTe multiple electrode detector." *Nucl. Instr. Methods Phys. Res. A*, Vol. 583, p. 324.

Abbene, L. et al. (2015), "Digital performance improvements of a CdTe pixel detector for high flux energy-resolved X-ray imaging," *Nucl. Instr. Methods Phys. Res. A*, Vol. 777, p. 54.

Allison, J. et al. (2016), "Recent developments in GEANT4", *Nucl. Instr. Methods Phys. Res. A*, Vol. 835, p. 186. GEANT 4 home page.

Antier, S. et al. (2015), "Hard X-ray polarimetry with Caliste, a high performance CdTe based imaging spectrometer," *Exp Astron*., Vol. 39, p. 233, DOI 10.1007/s10686-015-9442-5.

Auricchio N. et al. (1999), "Investigation of response behaviour in CdTe detectors versus inter-electrode charge formation position", *IEEE Trans. Nucl. Sci.,* Vol. 46, p. 853.

Auricchio, N. et al. (2005), "Twin shaping filter techniques to compensate the signals from CZT/CdTe detectors", *IEEE Trans. Nucl. Sci.,* Vol. 52, p. 1982.

Auricchio, N. et al. (2012), "Development status of a CZT spectrometer prototype with 3D spatial resolution for hard X ray astronomy", *Proc. SPIE*, Vol. 8453, p. 84530S.

Bale, D.S. and Szeles, C. (2006), "Design of high performance CdZnTe quasi-hemispherical gamma-ray CAPture™ plus detectors", *Proc. SPIE*, Vol. 6319, p. 63190B.

Barrett, H.H. et al. (1995), "Charge transport in arrays of semiconductor gamma-rays detectors," *Phys. Rev. Lett*., Vol. 75, p. 156.

Bellazzini, R. et al. (2010), *X-ray Polarimetry: A New Window in Astrophysics*, Cambridge University Press.

Berger, M.J. et al. (2010), "XCOM: Photon Cross Sections Database," http://www.nist.gov/pml/data/xcom/index.cfm.

Blozer, P. F. et al. (2016), "A concept for a soft gamma-ray concentrator using thin-film multilayer structures," *Proc. SPIE*, Vol. 9905, p. 99056L.

Bolotnikov, A.E. et al. (2006), "Performance characteristics of Frisch-ring CdZnTe detectors," *IEEE Trans. Nucl. Sci*., Vol. 53, p. 607.

Boucher, Y.A. et al. (2011), "Measurements of gamma rays above 3 MeV using 3D position-sensitive 20×20×15 mm^3 CdZnTe detectors," 2011 *IEEE Nucl. Sci. Symp. Conference Rec*., p. 4540.

Caroli, E. et al., (2000), "CIPHER: coded imager and polarimeter for high-energy radiation," *Nucl. Instr. Methods Phys. Res. A*, Vol. 448, p. 525.

Caroli, E. et al. (2002), "PolCA (Polarimetria con CdTe Array)," IASF/CNR Internal Report n. 345.

Caroli, E. et al. (2008), "A three-dimensional CZT detector as a focal plane prototype for a Laue Lens telescope," *Proc. SPIE*, Vol. 7011, p. 70113G.

Caroli, E. et al. (2009), "A polarimetric experiment with a Laue Lens and CZT pixel detector," *IEEE Trans. Nucl. Sci*., Vol. 56, p. 1848.

Caroli, E. et al. (2010), "Development of a 3D CZT detector prototype for Laue Lens telescope," *Proc. SPIE*, Vol. 7742, p. 77420V.

Caroli, E., and Del Sordo, S., (2015), "CdTe/CZT Spectrometers with 3-D Imaging Capabilities," in *Solid-State Radiation Detectors—Technology and Applications*, Awadalla, S. and Iniewski, K. (eds.), CRC Press (Boca Baton, London, New York), ISBN: 978-1-4822-6221-6.

Caroli, E. et al. (2015), "Monte Carlo evaluation of a CZT 3D spectrometer suitable for a hard X- and soft-γ rays polarimetry balloon borne experiment," 2015 IEEE Conf Records, DOI: 10.1109/NSSMIC.2015.7582278.

Casali, F. et al. (1992), "Characterization of small CdTe detectors to be used for linear and matrix arrays," *Nucl. IEEE Trans. Nucl. Sci.,* Vol. 39, p. 598.

Cavalleri, G. et. al. (1971), "Extension of Ramo theorem as applied to induced charge in semiconductor detectors," *Nucl. Instr. Methods Phys. Res.,* Vol. 92, p. 137.

Chauvin, M. et al. (2016), "Optimising a balloon-borne polarimeter in the hard X-ray domain: From the PoGOLite Pathfinder to PoGO+," *Astroparticle Phys.*, Vol. 82, p. 99.

Curado da Silva, R.M. et al. (2003), "CIPHER, a polarimeter telescope concept for Hard X-ray Astronomy," *Exp. Astron.*, Vol. 15, p. 45.

Curado da Silva, R.M. et al. (2004), "Hard-X and soft gamma-ray polarimetry with CdTe array prototypes," *IEEE Trans. Nucl. Sci.,* Vol. 51, p. 2478.

Curado da Silva, R.M. et al. (2008), "Polarimetric performance of a Laue lens gamma-ray CdZnTe focal plane prototype," *J. Appl. Phys.,* Vol. 104, p. 084903.

Curado da Silva, R.M. et al. (2011), "Polarimetry study with a CdZnTe focal plane detector," *IEEE Trans. Nucl. Sci.*, Vol. 58, p. 2118.

Curado da Silva, R.M. (2012), "Polarization degree and direction angle effects on a CdZnTe focal plane performance," *IEEE Trans. Nucl. Sci.*, Vol. 59, p. 1628.

Cui, Y. et al. (2008), "Hand-held gamma-ray spectrometer based on high-efficiency Frisch-ring CdZnTe detectors," *IEEE Trans. Nucl. Sci.*, Vol. 55, p. 2765.

Dean, A.J. et al. (2008), "Polarized gamma ray emission from the CRAB," *Science*, Vol. 321, no 5893, p. 1183.

Della Monica Ferreira, D. et al. (2013), "Hard X-ray/soft gamma-ray telescope designs for future astrophysics missions," *Proc. SPIE*, Vol. 886, p. 886116-1

De Geronimo, G. et al. (2003), "Advanced-readout ASICs for multielement CdZnTe detectors," *Proc. SPIE*, Vol. 4784, p. 105, 2003.

Devanathan, R. et al. (2006), "Signal variance in gamma-ray detectors—A review," *Nucl. Instr. Methods Phys. Res. A*, Vol. 565, p. 637.

Dish, C. et al. (2010), "Coincidence measurements with stacked (Cd,Zn)Te coplanar grid detectors," IEEE Nucl. Sci. Symp. Conference Record, p. 3698.

Du, Y.F. et al. (2001), "Evaluation of a Compton scattering camera using 3-D position sensitive CdZnTe detectors," *Nucl. Instr. Methods Phys. Res. A*, Vol. 457, p. 203.

ESRF (2017), European Synchrotron Research Facility (Grenoble, France): http://www.esrf.eu/UsersAndScience.

Eberth, J. and Simpson, J. (2006), "From Ge(Li) detectors to gamma-ray tracking arrays—50 years of gamma spectroscopy with germanium detectors," *Prog. Particle Nucl. Phys.,* Vol. 60, p. 283.

Eskin, J.D. et al. (1999), "Signals induced in semiconductor gamma-ray imaging detectors," *J. Appl. Phys.,* Vol. 85, p. 647.

Forot, M. et al. (2008), "Polarization of the crab pulsar and nebula as observed by the INTEGRAL/IBIS telescope," *Ap. J.*, Vol. 688, p. L29.

Frisch, O., (1944), British Atomic Energy Report, BR-49.

Frontera, F. et al. (2013), "Scientific prospects in soft gamma-ray astronomy enabled by the LAUE project," *Proc. SPIE*, Vol. 8861, p. 886106-1.

Gostilo, V. et al. (2002), "The development of drift-strip detectors based on CdZnTe," *IEEE Trans. Nucl. Sci.*, Vol. 49, p. 2530.

Götz, D. et al. (2009), "Variable polarization measured in the prompt emission of GRB 041219A using IBIS on board INTEGRAL," *Astrophys. J. Lett.*, Vol. 695, p. 2.
Gu, Y. et al. (2011), "Study of a high-resolution, 3D positioning cadmium zinc telluride detector for PET," *Phys. Med. Biol.*, Vol. 56, p. 1563.
Guazzoni, G. et al. (1991), "A mixer unit for data acquisition," *Nucl. Instr. Methods Phys. Res. A*, Vol. 305, p. 442
He, Z. et al. (1999), "3-D position sensitive CdZnTe gamma-ray spectrometers," *Nucl. Instr. Methods Phys. Res. A*, Vol. 422, p. 173.
He, Z. (2001), "Review of the Shockley–Ramo theorem and its application in semiconductor gamma ray detectors," *Nucl. Instr. Methods Phys. Res. A*, Vol. 463, p. 250.
He, Z. et al. (1997), "Position-sensitive single carrier CdZnTe detectors," *Nucl. Instr. Methods Phys. Res. A*, Vol. 388, p. 180.
Hecht, K. (1932), "Zum Mechanismus des lichtelektrischen Primärstromes in isolierenden Kristallen," *Z. Phys.*, Vol. 77, p. 235.
IDL 2017, Interactive Data Language from Harris Geospatial Solution: http://www.exelisvis.it/ProdottieServizi/IDL.aspx
Jordanov, V.T. et. al. (1996) "Compact circuit for pulse rise-time discrimination," *Nucl. Instr. Methods Phys. Res. A*, Vol. 380, p. 353.
Judson, D.S. et al. (2011) "Compton imaging with the PorGamRays spectrometer," *Nucl. Instr. Methods Phys. Res. A*, Vol. 652, p. 587.
Kim, H. et al. (2004), "Investigation of the energy resolution and charge collection efficiency of Cd(Zn)Te detectors with three electrodes," *IEEE Trans. Nucl. Sci.*, Vol. 51, p. 1229.
Kislat, F. et al. (2017), "Design of the telescope truss and gondola for the balloon-borne X-ray polarimeter X-Calibur," submitted to *J. Astronom. Instrument.*, arXiv:1511.02735v2.
Knödlseder, J. et al. (2007), "GRI: focusing on the evolving violent universe," *Proc. SPIE*, Vol. 6688, p. 668806.
Kole, M. et al. (2016), "POLAR: Final calibration and in-flight pEE NSS/MIC Conf. in Strasbourg (F), 29 Oct.–5 Nov. 2016, arXiv:1612.04098v1.
Kozorezov, A.G. et al. (2005), "Resolution degradation of semiconductor detectors due to carrier trapping," *Nucl. Instr. Methods Phys. Res. A*, Vol. 546, p. 207.
Kroeger, R.A. et al. (1996), "Gamma-ray instrument for polarimetry, spectroscopy, and imaging (GIPSI)," *Proc. SPIE*, Vol. 2806, p. 52.
Kuvvetli, I., and Budtz-Jørgensen, C. (2005), "Pixelated CdZnTe drift detectors," *IEEE Trans. Nucl. Sci.*, Vol. 52, p. 1975.
Kuvvetli, I. et al. (2010a), "CZT drift strip detectors for high energy astrophysics," *Nucl. Instr. Methods Phys. Res. A*, Vol. 624, p. 486.
Kuvvetli, I. et al. (2010b), "Charge collection and depth sensing investigation on CZT drift strip detectors," IEEE Nucl. Sci. Symp. Conference Record, p. 3880.
Kuvvetly, I. et al. (2014), "A 3D CZT high resolution detector for x-and gamma-ray astronomy," *Proc. SPIE*, Vol. 9154, p. 91540X-1, doi: 10.1117/12.2055119.
Laurent, P. et al. (2011), "Polarized gamma-ray emission from the galactic black hole Cygnus X-1," *Science*, Vol. 332, p. 438.
Lebrun, F. et al. (2003), "ISGRI: The INTEGRAL soft gamma-ray imager," *Astron. Astrophys.*, Vol. 411, p. L141.
Lechner, P. et al. (2004), "Novel high-resolution silicon drift detectors," *X Ray Spectrometr.*, Vol. 33, p. 256.

Lee, K. et al. (2010), "Development of X-ray and gamma-ray CZT detectors for Homeland Security Applications," *Proc. SPIE*, Vol. 7664, p. 766423-1.

Lei, F. et al. (1997), "Compton polarimetry in gamma-ray astronomy," *Space Sci. Rev.*, Vol. 82, p. 309.

Leo, W.R., *Techniques for Nuclear and Particle Physics Experiments*, Springer-Verlag (Berlin, Heidelberg), ISBN 978-3-642-57920-2 (1994).

Li, W. et al. (1999), "A data acquisition and processing system for 3-D position sensitive CZT gamma-ray spectrometers," *IEEE Trans. Nucl. Sci.*, Vol. 46, p. 1989.

Li, W. et al. (2000), "A modeling method to calibrate the interaction depth in 3-D position sensitive CdZnTe gamma-ray spectrometers," *IEEE Trans. Nucl. Sci.,* Vol. 47, p. 890.

Limousin, O. et al. (2011), "Caliste-256: A CdTe imaging spectrometer for space science with a 580 μm pixel pitch. *Nucl. Instr. Methods Phys. Res. A*, Vol. 647, p. 46.

Lingren, C.L. et al. (1998), "Cadmium-zinc telluride, multiple-electrode detectors achieve good energy resolution with high sensitivity at room-temperature," *IEEE Trans. Nucl. Sci.,* Vol. 45, p. 433.

Luke, P.N. (1995), "Unipolar charge sensing with coplanar electrodes—Application to semiconductor detectors," *IEEE Trans. Nucl. Sci.,* Vol. 42, p. 207.

Luke, P.N. (2000), "Coplanar-grid CdZnTe detector with three-dimensional position sensitivity," *Nucl. Instr. Methods Phys. Res. A*, Vol. 439, p. 611.

Macri, J.R. et al. (2002), "Study of 5 and 10 mm thick CZT strip detectors," 2002 IEEE Nucl. Sci. Symp. Conference Record, p. 2316.

Macri, J.R. et al. (2003), "Readout and performance of thick CZT strip detectors with orthogonal coplanar anodes," 2003 IEEE Nucl. Sci. Symp. Conference Record, p. 468.

Matteson, J.L. et al. (2003), "CZT detectors with 3-D readout for gamma-ray spectroscopy and imaging," *Proc. SPIE*, Vol. 4784. Doi: 10.1117/12.455978.

McConnell, M. et al. (2009), "X-ray and gamma-ray polarimetry," Astro2010: The Astronomy and Astrophysics Decadal Survey, Science White Papers, no. 198.

McGregor, D.S. et al. (1998), "Single charge carrier type sensing with a parallel strip pseudo-Frisch-Grid CdZnTe semiconductor radiation detector," *Appl. Phys. Lett*., Vol. 12, p. 192.

Mihailescu, L. et al. (2007), "SPEIR: A Ge Compton camera," *Nucl. Instr. Methods Phys. Res. A*, Vol. 570, p. 89.

Ogawa, K., and Muraishi, M. (2010), "Feasibility study on an ultra-high-resolution SPECT with CdTe detectors," *IEEE Trans. Nucl. Sci.,* Vol. 57, p. 17.

Owens, A., and Peacock, A (2004), "Compound semiconductor radiation detectors," *Nucl. Instr. Methods Phys. Res. A*, Vol. 531, p. 18.

Owens, A. et al. (2006), "Hard X- and g-ray measurements with a large volume coplanar grid CdZnTe detector," *Nucl. Instr. Methods Phys. Res. A*, Vol. 563, p. 242.

Pantazis, T. et al. (2010), "The historical development of the thermoelectrically cooled X-ray detector and its impact on the portable and hand-held XRF industries," *X-Ray Spectrosc*., Vol. 39, p. 90.

Perillo, E. et al. (2004), "Spectroscopic response of a CdTe microstrip detector when irradiated at various impinging angles," *Nucl. Instr. Methods Phys. Res. A*, Vol. 531, p. 125.

Richter, M., and Siffert P. (1992), "High resolution gamma ray spectroscopy with CdTe detector systems," *Nucl. Instr. Methods Phys. Res. A*, Vol. 322, p. 529.

Shor, A. et al. (1999), "Optimum spectroscopic performance from CZT γ- and X-ray detectors with pad and strip segmentation," *Nucl. Instr. Methods Phys. Res. A*, Vol. 428, p. 182.
Sato, G. et al. (2002), "Characterization of CdTe/CdZnTe detectors," *IEEE Trans. Nucl. Sci.,* Vol. 49, p. 1258.
Tatischeff, V. et al. (2016), "The e-ASTROGAM gamma-ray space mission," *Proc. SPIE*, Vol. 9905, p. 99052N.
Stahle, C.M. et al. (1997), "Fabrication of CdZnTe strip detectors for large area arrays," *Proc. SPIE*, Vol. 315, p. 90,
Suffert, P.M. et al. (1959), "Polarization measurements of proton capture gamma rays," *Physica*, Vol. 25, p. 659.
Ubertini, P. et al. (2003), "IBIS: The Imager on-board INTEGRAL," *Astron. Astr.*, Vol. 411, p. L131.
Vetter, K. et al. (2007), "High-sensitivity Compton imaging with position-sensitive Si and Ge detectors," *Nucl. Instr. Methods Phys. Res., A*, Vol. 579, p. 363.
Virgilli, E. et al. (2015), "Hard x-ray broad band Laue lenses (80–600 keV): Building methods and performances," *Proc. SPIE*, Vol. 9603, p. 960308-1.
Von Ballmoos, P. et al. (2010), "A DUAL mission for nuclear astrophysics," *Nucl. Instr. Methods*, Vol. A623, p. 431.
Wahl, C.G. and He, Z. (2011), "Gamma-ray point-source detection in unknown background using 3D-position-sensitive semiconductor detectors," *IEEE Trans. Nucl. Sci.*, Vol. 58, p. 605.
Whal, C.G. et al. (2015), "The Polaris-H imaging spectrometer," *Nucl. Instr. Methods Phys. Res., A* Vol. 784, p. 377.
Watanabe, S. et al. (2002), "CdTe stacked detectors for gamma-ray detection," *IEEE Trans. Nucl. Sci.*, Vol. 49, p. 1292.
Watanabe, S. et al. (2009), "High energy resolution hard X-ray and gamma-ray imagers using CdTe diode devices," *IEEE Trans. Nucl. Sci.*, Vol. 56, p. 777.
Weisskopf, M.C. et al. (2009), "The prospects for X-ray polarimetry and its potential use for understanding neutron stars," *Neutron Stars Pulsars Astrophys. Space Sci. Lib.,* Vol. 357, p. 589.
Winkler, C. et al. (2003), "The integral mission," *Astron. Astr.*, Vol. 411, p. L1.
Xu, D. et al. (2004), "4π Compton imaging with single 3D position sensitive CdZnTe detector," *Proc. SPIE*, Vol. 5540, p. 144.
Xu, D. et al. (2005), "Detection of gamma ray polarization using a 3-D position-sensitive CdZnTe detector," *IEEE Trans. Nucl. Sci.*, Vol. 52, p. 1160.
Zanichelli, M. et al. (2013), "Charge collection in semi-insulator radiation detectors in the presence of a linear decreasing electric field," *J. Phys. D: Appl. Phys.*, Vol. 46, p. 365103.
Zhang, F. et al. (2004), "Improved resolution for 3-D position sensitive CdZnTe Spectrometers," *IEEE Trans. Nucl. Sci.*, Vol. 51, p. 2427.
Zhang, F. et al. (2012), "Characterization of the H3D ASIC readout system and 6.0 cm 3-D position sensitive CdZnTe detectors," *IEEE Trans. Nucl. Sci.*, Vol. 59, p. 236.